1
Magnets for Accelerators

If you want to build a ship, don't herd people together
to collect wood and don't assign them to tasks and work,
but rather teach them to long for the endless immensity of the sea.

Antoine de Saint-Exupéry (1900–1944).

A number of comprehensive books have been published on the design and construction of accelerator magnets, for example, by Wilson [68], Brechna [17], Meß, Schmüser, and Wolff [51], Iwasa [34], and Asner [2]. Other sources of information are the proceedings of the Magnet Technology (MT) conferences, which are usually published in the *IEEE Transactions on Applied Superconductivity*. The large amount of publications is not surprising inasmuch as the magnet systems and the cryogenic installations are the most expensive components of circular high-energy particle accelerators.

Like previous projects in high-energy physics, the *Large Hadron Collider* (LHC), built at CERN in Geneva, Switzerland, has greatly benefited from the developments in superconductivity and cryogenics. In turn, these fields have enormously gained through the R&D undertaken by CERN in collaboration with industry and national institutes, as well as by the production of components on an industrial scale.

This book concentrates on the mathematical foundations of field computation and its application to the electromagnetic design of accelerator magnets and solenoids. It is fitting, then, that we should briefly review a number of technological challenges that had to be met for the design, manufacture, construction, installation, and commissioning of the LHC main ring. A good overview is given in [27]. Challenges are found in all domains of physics and engineering. They comprise, among others:

- Material science aspects, such as the development of superconducting wires and cables, the specification of austenitic and magnetic steel, and the choice of radiation resistant insulation, among others.
- Mechanical engineering challenges, such as finding the appropriate force-restraining structure for the coils, the right level of prestress in

Field Computation for Accelerator Magnets. Stephan Russenschuck

ISBN: 978-3-527-40769-9

the coil/collar assembly, the design of manufacturing tooling, coldmass integration and welding techniques, cryostat integration, and magnet installation and interconnection, all made more difficult by the very tight tolerances required by the optics of the particle beam.
- The physics of superfluid helium and cryogenic engineering for helium distribution lines, refrigeration, and process control.
- Vacuum technology for insulation and the beam vacuum. The beam vacuum system must provide adequate beam lifetime in a cryogenic system, where heat flow to the 1.9 K helium circuit must be minimized.
- Metrology for magnet alignment in the tunnel.
- Electrical engineering challenges for power supplies (high current, low voltage), water-cooled cables, current leads using high T_c superconductors, superconducting busbars, diodes operating at cryogenic temperatures, magnet protection and energy extraction systems, and powering interlocks.
- Magnetic field quality measurements and powering tests.

We will review these engineering aspects after a brief introduction to the LHC project. Finally, we will turn to the challenges of electromagnetic design, which required the development of dedicated software for numerical field computation.

1.1
The Large Hadron Collider

With the Large Hadron Collider (LHC), the particle physics community aims at testing various grand unified theories by studying collisions of counter-rotating proton beams with center-of-mass energies of up to 14 teraelectronvolt (TeV). Physicists hope to prove the popular *Higgs mechanism*[1] for generating elementary particle masses of the quarks, leptons, and the W and Z bosons. Other research concerns supersymmetric (SUSY) partners of the particles, the apparent violations of the symmetry between matter and antimatter (CP-violation), extra dimensions indicated by the theoretical gravitons, and the nature of dark matter and dark energy. A general overview of this topic is given in [36].

The exploration of rare events in the LHC collisions requires both high beam energies and high beam intensities. The high beam intensities exclude the use of antiproton beams and thus imply two counter-rotating proton beams, requiring separate beam pipes and magnetic guiding fields of opposite polarity. Common sections are located only at the four *insertion regions* (IR), where

---

[1] Peter Higgs, born in 1929.

the experimental detectors are located. The large number of bunches, 2808 for each proton beam, and a nominal bunch spacing of 25 ns creates 34 "parasitic" collision points in each experimental IR. Thus dedicated orbit bumps separate the two LHC beams left and right from the *interaction point* (IP) in order to avoid the parasitic collisions at these points. The number of events per second, generated in the LHC collisions, is given by $N = L\sigma$, where σ is the interaction cross section for the event and L the *machine luminosity*, $[L] = 1\ \mathrm{cm}^{-2}\,\mathrm{s}^{-1}$. In scattering theory and accelerator physics, luminosity is the number of events per unit area and unit time, multiplied by the opacity of the target. The machine luminosity of a collider depends only on the beam parameters and can be written for a Gaussian[2] beam distribution as

$$L = \frac{N_\mathrm{b}^2 n_\mathrm{b} f \gamma}{4\pi \epsilon_n \beta^*} F\,, \tag{1.1}$$

where N_b is the number of particles per bunch, n_b the number of bunches per beam, f the revolution frequency, γ the relativistic gamma factor, ϵ_n the normalized transverse beam emittance, and β^* the beta function at the collision point. The factor F accounts for the reduction of luminosity due to the crossing angle at the interaction point (IP):

$$F = \left(1 + \left(\frac{\theta \sigma_z}{2\sigma^*}\right)^2\right)^{-\frac{1}{2}}\,, \tag{1.2}$$

where θ is the full crossing angle at the interaction point, σ_z the RMS bunch length, and σ^* the transverse RMS beam size at the interaction point. All the above expressions assume equal beam parameters for the two circulating beams.

Two high-luminosity experiments, ATLAS [6] and CMS [20], aiming at a peak luminosity[3] of $10^{34}\ \mathrm{cm}^{-2}\,\mathrm{s}^{-1}$, will record the results of the particle collisions. In addition, the LHC has two low-luminosity experiments: LHCB [45] for B-physics aiming at a peak luminosity of $10^{32}\ \mathrm{cm}^{-2}\,\mathrm{s}^{-1}$ and TOTEM [63] for the detection of protons from elastic scattering at small angles aiming at a peak luminosity of $2 \times 10^{29}\ \mathrm{cm}^{-2}\,\mathrm{s}^{-1}$ for 156 bunches. LHCf is a special-purpose experiment for astroparticle physics. A seventh experiment, FP420, has been proposed that would add detectors to available spaces located 420 m on either side of the ATLAS and CMS detectors.

The LHC will also be able to collide heavy ions, such as lead ions, up to an energy level of about 1100 TeV. These collisions cause the phase transition of nuclear matter into quark-gluon plasma as it existed in the very early universe

[2] Carl Friedrich Gauss (1777–1855).

[3] The luminosity is not constant during a physics run, but decays due to the degradation of intensity and emittance of the beam.

around 10^{-6} s after the Big Bang. Heavy-ion physics is studied at the ALICE experiment. ALICE [7] aims at a peak luminosity of 10^{27} cm^{-2} s^{-1} for nominal Pb–Pb ion operation.

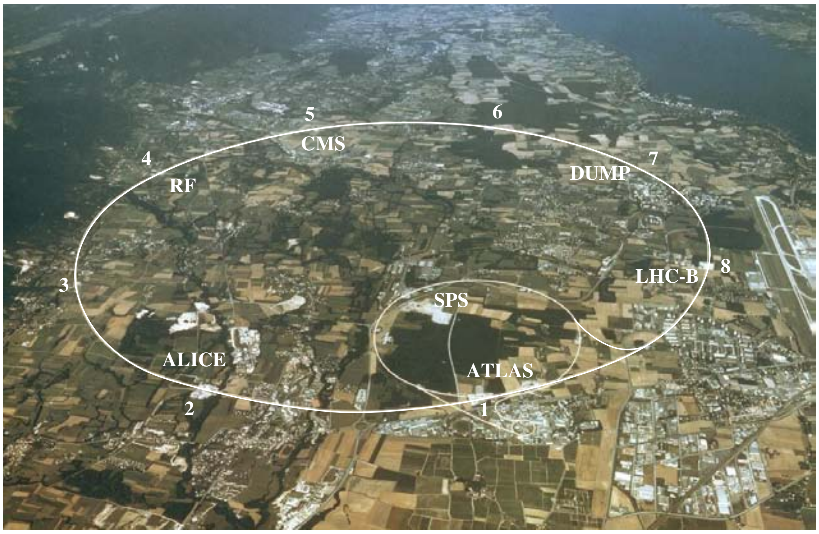

Figure 1.1 Layout of the LHC main ring with its physics experiments ATLAS, CMS, ALICE, LHC-B, and the radio frequency and beam dump insertions at IP 4 and 7.

The LHC reuses the civil engineering infrastructure of the Large Electron Positron Collider (LEP), which was operated between 1989 and 2000. The tunnel with a diameter of 3.8 m and a circumference of about 27 km straddles the Swiss/French boarder near Geneva, at a depth between 50 and 175 m underground. The layout of the LHC main ring with its physics experiments is shown in Figure 1.1. With a given circumference of the accelerator tunnel, the maximum achievable particle momentum is proportional to the operational field in the bending magnets. Superconducting dipole magnets cooled to 1.9 K, with a nominal field of 8.33 T, allow energies of up to 7 TeV per proton beam.[4]

A hypothetical 7 TeV collider using normal-conducting magnets, with a field limited to 1.8 T by the saturation of the iron yoke, would be 100 km in circumference. Moreover, it would require some 900 MW of electrical power, dissipated by ohmic heating in the magnet coils, instead of the 40 MW used by the cryogenic refrigeration system[5] of the superconducting LHC machine [42]. The operational magnetic field in the string of superconducting magnets de-

---

[4] The conversion to degrees Celsius is $\{T\}_{°\mathrm{C}} = \{T\}_{\mathrm{K}} - 273.16$.

[5] According to a National Institute of Standards and Technology (NIST) convention, cryogenics involves temperatures below −180 °C (93.15 K), i.e., below the boiling points of freon and other refrigerants.

pends, however, on the heat load and temperature margins of the cryomagnets and therefore on the beam losses in the machine during operation. Operating the superconducting magnets close to the *critical surface* of the superconductor therefore requires efficient operation with minimal beam losses.

The two counter-rotating beams require two separate magnetic channels with opposite magnetic fields.[6] The available space in the LHC tunnel does not allow for two separate rings of cryomagnets as was planned for the superconducting supercollider (SSC) [57]. The LHC main dipole and quadrupole magnets are twin-aperture designs with two sets of coils and beam channels within a common mechanical structure, iron yoke, and cryostat. The dipole cross section is shown in Figure 1.15. The distance between the beam channels is 194 mm at operational temperature.

The eight arcs of the LHC are composed of 23 regular arc-cells, each 106.9 m long, of the so-called *FODO structure* schematically shown in Figure 1.2. Each cell is made of two identical half-cells, each of which consists of a string of three 14.3-m-long main dipoles (MB) and one 3.10-m-long main quadrupole (MQ). Sextupole, decapole, and octupole correctors are located at the ends of the main dipoles. The quadrupoles are housed in the *short straight sections* (SSS), which also contain combined sextupole/dipole correctors, octupoles or trim quadrupoles, and beam position monitors. The role of the different correctors will be discussed in Chapter 11.

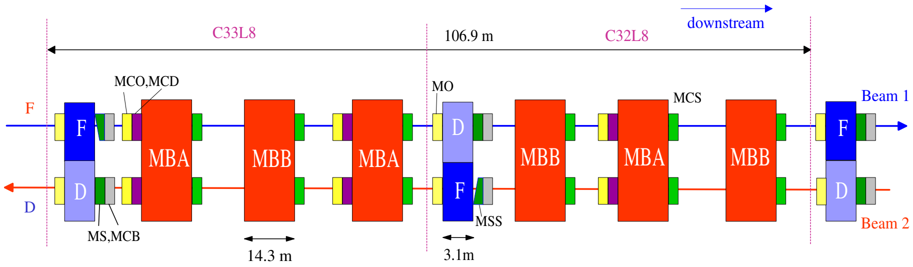

Figure 1.2 Layout of the FODO cells of the LHC main ring. Multipole corrector magnets are connected to the main dipoles (MBA and MBB), and lattice correctors are connected to the main quadrupoles in the short straight section (SSS). The lengths of the magnets are not to scale.

The two coil pairs in the dipole magnets are powered in series, and therefore all dipole magnets in one arc form a single electrical circuit. The quadrupoles in each arc form two electrical circuits: All focusing quadrupole magnets for Beam 1 and Beam 2 are powered in series (see Chapter 12), and all defocusing quadrupole magnets for both beams are powered in series. The optics

---

[6] Beam 1 is defined as the clockwise circulating beam (seen from above), while Beam 2 circulates anticlockwise.

of Beam 1 and Beam 2 in the arc cells are therefore strictly coupled, via the powering of the main magnetic elements.

The eight *long straight sections*, each approximately 528 m long, are available for experimental insertions or utilities. IR 2 contains the injection systems for Beam 1, while the counter-rotating Beam 2 is fed into the LHC at IR 8. The insertion regions 3 and 7 each contain two *beam collimation systems* and use normal-conducting magnets that are more robust against the inevitable beam loss on the primary collimators. Insertion region 4 contains the radio frequency systems.

A total beam current of 0.584 A corresponds to a stored energy of approximately 362 MJ. This stored energy must be absorbed safely at the end of each physics run, in the event of a magnet quench or an emergency. At IR 6 the beams are extracted vertically from the machine using a combination of horizontally deflecting, fast-pulsed kicker magnets and vertically deflecting, normal-conducting septum magnets. In addition to the energy stored in the circulating beams, the LHC magnet system has a stored electromagnetic energy of approximately 600 MJ. As part of the magnet-protection system, an energy extraction system consisting of switches and *protection resistors* is installed outside the continuous cryostat.

Remanent magnetic fields in the bending magnets (from iron magnetization in normal-conducting magnets or superconducting filament magnetization in superconducting magnets) make it impossible to ramp accelerator magnets linearly from an arbitrarily small field level. The LHC uses an existing injector chain that includes many accelerators at CERN: The linear accelerator Linac 2 generates 50 MeV protons and feeds the Proton Synchrotron Booster (PSB). Protons are then injected at 1.4 GeV into the Proton Synchrotron (PS) where they are extracted at 26 GeV. The Super Proton Synchrotron (SPS) is used to increase the energy of protons to the LHC injection energy of 450 GeV.

Filling the LHC requires 12 cycles of the SPS and each SPS fill requires three to four cycles of the PS. The total LHC filling takes approximately 16 min. The minimum time required for ramping the beam energy in the LHC from 450 GeV to 7 TeV is approximately 20 min. After a beam abort at top energy it also takes 20 min to ramp the magnets down to the injection field level. Allowing for a 10 min check of all main systems, one obtains a theoretical turnaround time for the LHC of 70 min.[7]

[7] The average time between the end of a luminosity run and a new beam at top energy in the HERA accelerator was about 6 h, compared to a theoretical minimum turnaround time of approximately 1 h.

A relativistic particle of charge e and mass m forced to move along a circular trajectory loses energy by emission of photons (synchrotron radiation) according to

$$\Delta E = \frac{1}{3\varepsilon_0} \frac{e^2 E^4}{(mc^2)^4 R}\,, \tag{1.3}$$

with every turn completed [66]. In Eq. (1.3), $\varepsilon_0 = 8.8542\ldots \times 10^{-12}\ \mathrm{F\,m^{-1}}$ is the permittivity of free space, R the radius of curvature of the particle trajectory, E the particle's energy, and c the speed of light in vacuum. A comparison between electron and proton beams of the same energy yields

$$\frac{\Delta E_\mathrm{p}}{\Delta E_\mathrm{e}} = \left(\frac{m_\mathrm{e} c^2}{m_\mathrm{p} c^2}\right)^4 = \left(\frac{0.511\,\mathrm{MeV}}{938.19\,\mathrm{MeV}}\right)^4 = 8.8 \times 10^{-14}. \tag{1.4}$$

Although the synchrotron radiation in hadron storage rings is small compared to that generated in electron rings, it still imposes practical limits on the maximum attainable beam intensities, as the radiation must be absorbed in a cryogenic system. This affects the installed power of the refrigeration system and is an important cost issue. Moreover, the synchrotron light impinges on the beam pipe walls in the form of a large number of hard UV photons. These in turn release absorbed gas molecules, which increase the residual gas pressure and liberate electrons; these are accelerated across the beam pipe by the positive electric field of the proton bunches.

The particle momentum in units of $\mathrm{GeV\,c^{-1}}$ is given by[8]

$$\{p_0\}_{\mathrm{GeV\,c^{-1}}} \approx 0.3\,\{R\}_\mathrm{m}\,\{B_0\}_\mathrm{T}. \tag{1.5}$$

The term $B_0 R$ is called the *magnetic rigidity* and a measure of the beam's stiffness in the bending field. For the LHC it is 1500 T m at injection and 23 356 T m at collision energy.

Table 1.1 shows a comparison of the maximum proton beam energy of different particle accelerators and the maximum flux density in the superconducting dipole magnets. Note that the effective radius is between 60% and 70% of the tunnel radius because of the dipole *filling factor* and the straight sections around the collision points.[9]

1.2
A Magnet Metamorphosis

The first superconducting magnets ever to be operated in an accelerator were the eight quadrupoles of the high-luminosity insertion at the CERN ISR [13].

---

[8] For a proof see Section 11.2.

[9] The filling factor is less than one because of dipole-free regions in the interconnections, space requests for focusing elements, etc.

Table 1.1 Comparison of the maximum proton beam energy in particle accelerators and the maximum flux density in their bending magnets.

Accelerator	Tevatron	HERA	UNK	SSC	RHIC	LHC
Laboratory	FNAL	DESY	IHEP	SSCL	BNL	CERN
Commissioning	1983	1990	canceled	canceled	2000	2008
Country	USA	Germany	Russia	USA	USA	Switzerland
Circumference (km)	6.3	6.3	21	87.0	3.8	27.0
Proton momentum (TeV/c)	0.9	0.92	3.0	20.0	0.1	7.0
Nominal dipole flux density (T)	4.4	5.8	5.11	6.79	3.45	8.33
Injection dipole flux density (T)	0.66	0.23	0.69	0.68	0.4	0.535
Nominal current (A)	4400	5640	5073	6553	5050	11850
Number of dipoles per ring	774	416	2168	3972	264	1232
Aperture (mm)	76.2	75	80	50	80	56
Magnetic length (m)	6.1	8.8	5.8	15.0	9.7	14.312
Dipole filling factor	0.75	0.58	0.59	0.68	0.67	0.65

They used epoxy-impregnated coils with conductors made of a niobium–titanium (Nb–Ti) wire. Housed in independent cryostats equipped with vapor-cooled current leads, they operated in a saturated bath of liquid helium at 4.3 K.

The first completely superconducting accelerator was the Tevatron at FNAL (USA). This proton synchrotron, with a circumference of 6.3 km, comprises 774 superconducting dipoles and 216 superconducting quadrupoles, wound with conductors made of a Nb–Ti composite wire, and operated in forced-flow supercritical helium at 4.4 K. The Tevatron was later converted into a proton–antiproton collider and is still in operation.

Another superconducting synchrotron of comparable size was the proton ring of the electron–proton collider HERA at DESY (Germany) [65]. The LHC also builds on experience from the magnet design work for the SSC project (USA) that was canceled in 1993 [57].

Figure 1.3 (left) shows the HERA accelerator tunnel at DESY, where a ring (bottom) of normal-conducting magnets steers the electron beam, and a ring of superconducting magnets (top) steers the counter-rotating 820 GeV proton beam. Its 416 superconducting dipoles (with a field of 5.2 T) and 224 quadrupoles were also wound with a Nb–Ti cable and operated in forced-flow supercritical helium at 4.4 K. Unlike those of the Tevatron, the magnets of HERA had their iron yoke positioned inside the helium vessel of the cryostat and therefore at cryogenic temperatures.

Now we will discuss the difference between normal– and superconducting magnets from the point of view of the electromagnetic design and optimization. To explain the design concepts and to account for some of the historical development of the technology, Figures 1.4–1.8 show the metamorphosis in the normal-conducting dipoles for LEP and two different designs of super-

Figure 1.3 Left: High Energy Ring Accelerator (HERA) at DESY [33], Hamburg, Germany, where in one ring the normal-conducting magnets steer the electron beam and in the other the superconducting magnets steer the counter-rotating proton beam. Right: LEP quadrupole and dipoles. The main dipoles have a bending field of 0.109 T at a beam energy of 100 GeV.

conducting twin-aperture magnets for counter-rotating high-energy proton beams.

All field calculations were performed using the CERN field computation program ROXIE, employing the numerical field methods described in Chapter 14. The color representation of the magnetic flux density in the iron yokes is identical in all cases, whereas the size of the field icons changes with the different field strengths. We always distinguish between the *source field* generated by the transport current in the coils alone, and the *total field* comprising both the coil field and the contribution from the iron yoke magnetization.[10] The total field, denoted B_t, is thus the sum of the source field B_s and the *reduced field* B_r. It is then easy to distinguish between iron-dominated and coil-dominated magnets. In the LHC dipole magnets the reduced field accounts only for around 20% of the total field; they are clearly coil-dominated.

As accelerator magnets are in general long with respect to the dimension of the aperture, we can limit ourselves here to 2D field computations. The effects of coil ends will be discussed in Chapters 15 and 19.

Figure 1.4 (left) shows the slightly simplified cross section of the C-shaped dipole of LEP. The advantage of C-shaped magnets is an easy access to the beam pipe. However, they have a higher fringe field and are mechanically less rigid than the H-type magnets as shown in Figure 1.4 (right). For the same air-gap flux, the iron yoke of the H-type magnet is smaller because the flux is guided through the two return paths. Additional pole shims can be mounted in order to improve the field quality in the aperture. The field of these magnets

[10] Somewhat casually we often use the word field synonymously for magnetic flux density.

is dominated by the shape of the iron yoke; in the case of the H-magnet the source field is only 0.065 T, compared to a total field of 0.3 T. Figure 1.3 (right) shows the C-shaped dipole magnets and a quadrupole installed in the LEP tunnel.

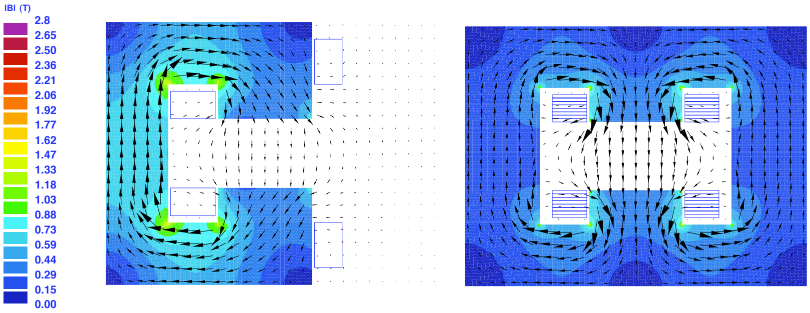

Figure 1.4 Left: C-shaped dipole of LEP ($N{\cdot}I = 2 \cdot 5250$ A, $B_\mathrm{t} = 0.13$ T, $B_\mathrm{s} = 0.042$ T). Filling factor of the yoke laminations of 0.27. Right: H-magnet as used in beam transfer lines. $N{\cdot}I = 24\,\mathrm{kA}$, $B_\mathrm{t} = 0.3$ T, the source field from the coils is only $B_\mathrm{s} = 0.065$ T, and the filling factor of the yoke laminations is 0.98.

The field quality in the aperture of the magnet is determined by the shape of the iron yoke and pole piece, which can be controlled by precision stamping of the laminations. Tolerances in the cable position have basically no effect on the magnetic field.

The LEP dipoles were ramped from 0.0218 T at injection energy (20 GeV) to 0.109 T at 100 GeV. In order to reduce the effect of remanent iron magnetization and achieve a more economical use of the steel, the yoke was laminated with a *stacking factor*[11] of only 0.27. The longitudinal spaces were filled with cement mortar, which ensured the mechanical rigidity of the yokes. This resulted, however, in unacceptable fluctuations in the bending field at low excitation, caused by the reduction of the maximum permeability due to *magnetostriction*. This phenomenon will be discussed in Section 4.6.4.

Superconducting technology allows the increase of the excitation current well above a density of 10 $\mathrm{A\,mm^{-2}}$, which is the practical limit for normal-conducting (water-cooled) coils for DC magnets.[12] Disregarding for the moment the superconductor-specific phenomena such as magnetization, flux creep, and resistive transition, we can consider *engineering current densities* that are hundred times higher than those in water-cooled copper or aluminum

---

[11] For a definition of the stacking factor see Section 4.6.3.

[12] Pulsed septum magnets are operated with current densities of up to 300 $\mathrm{A\,mm^{-2}}$.

coils.[13] Magnets in which the coils are superconducting but in which the magnetic field distribution is still dominated by the iron yoke are known as *superferric*. Figure 1.5 (left) shows a H-type magnet with increased excitation as can be achieved by superconducting coils. The poles are beginning to saturate, and the field quality in the aperture is degraded due to the increasing fringe field. An improved design, shown in Figure 1.5 (right), features tapered poles, a concave pole shape, and a small hole to equalize saturation effects during the field sweep from injection to nominal excitation.

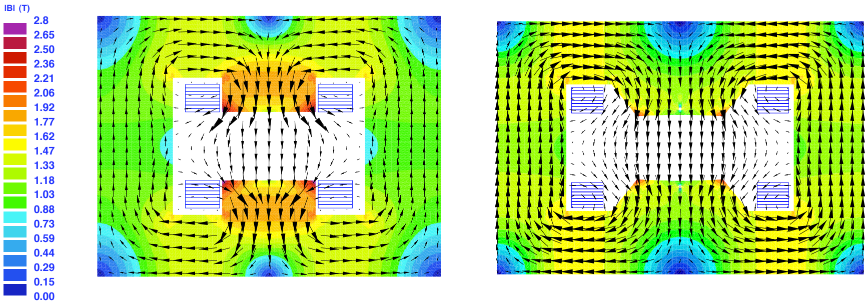

Figure 1.5 Left: H-magnet with increased excitation current ($N \cdot I = 96\ \mathrm{kA}$, $B_\mathrm{t} = 1.17$ T, $B_\mathrm{s} = 0.26$ T). Right: Improved design with tapered pole, concave pole shape, and a small hole to equalize iron saturation ($N \cdot I = 96\ \mathrm{kA}$, $B_\mathrm{t} = 1.15$ T, $B_\mathrm{s} = 0.208$ T).

Saturation of the pole can be avoided in window frame magnets as shown in Figure 1.6 (left). The disadvantage of window frame magnets is that synchrotron radiation is partly absorbed in the coils and access to the beam pipe is difficult. The advantages are that a better field quality is obtained and pole shims can be avoided. Superconducting window frame magnets have received considerable attention since the mid-1990s as a design alternative for high-field dipoles in the 14–16 T field range, taking advantage of easier coil winding and mechanical force retaining structures [31].

By superposition of two window frame magnets it is possible to increase the aperture field while reducing the magnetic flux density in the pole faces; see Figure 1.6 (right). A technical difficulty arises here in achieving the double current density in the square overlap area at the horizontal median plane [4].

At higher field levels, the field quality in the aperture of accelerator magnets is increasingly affected by the coil layout. It will be explained in Chapter 8 that a current distribution of $\cos n\varphi_\mathrm{c}$ within a shell centered at the origin creates a perfectly homogeneous $2n$-polar field in the aperture. An advantage of this design is that for the dipole, $n = 1$, the field drops with r^{-2} outside the shell

---

[13] The engineering current density is an overall current density considering cooper stabilization, filling factors, and insulation.

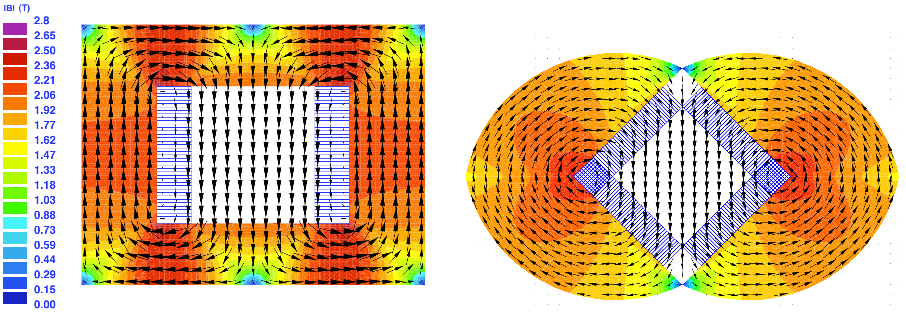

Figure 1.6 Left: Window frame geometry ($N{\cdot}I = 360\ \mathrm{kA}$, $B_\mathrm{t} = 2.0$ T, $B_\mathrm{s} = 1.04$ T). Notice the saturation of the poles in the H-magnet. Right: By superposition of two window frame magnets it is possible to increase the aperture field while reducing the magnetic flux density on the pole faces ($N{\cdot}I = 625\ \mathrm{kA}$, $B_\mathrm{t} = 2.38$ T, $B_\mathrm{s} = 1.36$ T).

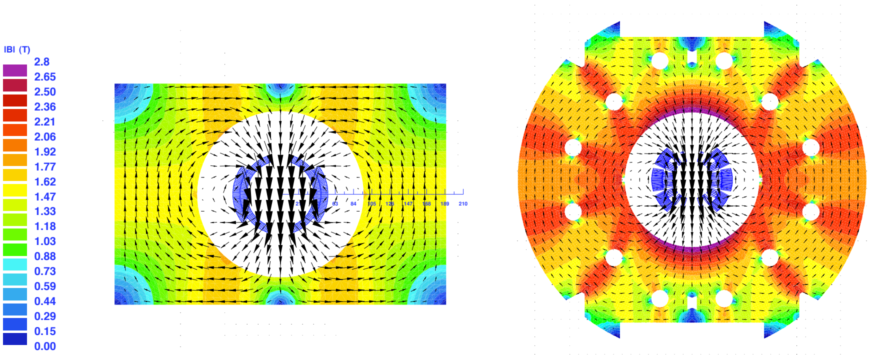

Figure 1.7 Left: Tevatron dipole with warm iron yoke and superconducting coil of the $\cos\varphi_\mathrm{c}$ type ($N{\cdot}I = 471\ \mathrm{kA}$, $B_\mathrm{t} = 4.16$ T, $B_\mathrm{s} = 3.39$ T). Notice that even with increased aperture field the flux density in the yoke is reduced due to the cos φ_c coil. Right: LHC single-aperture coil-test facility ($N{\cdot}I = 960\ \mathrm{kA}$, $B_\mathrm{t} = 8.33$ T, $B_\mathrm{s} = 7.77$ T).

and saturation effects in the iron yoke are reduced. Figure 1.7 (left) shows the magnets for the Tevatron accelerator at FNAL [25] with a coil design approximating the ideal $\cos\varphi_\mathrm{c}$ current distribution. The Tevatron dipole has an iron yoke at ambient temperature with the cryostat for the superconducting coil located inside the aperture of the yoke. The advantage of the solution is the low saturation in the yoke, up to the excitational limit set by the critical current of the superconductor. The disadvantage of the warm iron yoke is possible misalignment of the coil and its cryostat within the yoke, which is the source of unwanted multipole field errors. Misalignment also causes considerable net forces between the coil and the yoke, which requires many supports that increase the heat transfer from the warm iron yoke to the helium vessel. In addition, a passive quench protection system with parallel diodes is not easily implemented as it would require a parallel helium transfer line.

Figure 1.7 (right) shows the *coil-test facility* (CTF) used for validating the manufacturing process of the LHC magnets. The electromagnetic design of the CTF resembles the single-aperture dipole magnets proposed for the Superconducting Super Collider project, as well as the HERA and RHIC [60] dipoles. All these magnets feature iron yokes cooled to cryogenic temperatures, where the coil, collars, and yoke are enclosed in a helium-tight vessel, forming an assembly that is referred to as the *coldmass*. This principle was first developed for the main magnets of the ISABELLE project at Brookhaven and later adapted to the HERA accelerator magnets at DESY. This allows the positioning of the iron yoke closer to the superconducting coil and helps to increase the main field for a given amount of superconductor, while reducing the stored energy in the magnet. It also guarantees the centering of the coil and thus suppresses eccentricity forces on the coil. A disadvantage is the higher saturation-induced field distortion, which must be minimized using optimization methods coupled with FEM computations. Notice the large difference between the field in the aperture (8.3 T) and the field in the iron yoke (maximum 2.8 T) shown in Figure 1.7 (right). The iron yoke not only shields the stray fields, but also screens the beam from the influence of current busbars that are housed in groves on the outer rim of the iron yoke.

The source field generated by the superconducting coil alone is as high as 7.77 T and thus the magnetization of the iron yoke contributes only 10% to the total field. Higher contributions of the yoke magnetization to the central field can be obtained by replacing the collar with a fiberglass-phenolic spacer between the coil and yoke. This principle was used in the design of the RHIC dipole magnets in which the coil prestress was supplied by an outer cylindrical tube and the yoke laminations. This resulted in a 35% enhancement of the field due to the iron magnetization.

Figure 1.8 (left) shows the LHC main dipole in a twin-aperture design first proposed in [22]. It features two coils and two beam channels within a common mechanical structure and iron yoke. The mechanical structure and the cryostat are shown in Figure 1.15. The current-dependent multipole field errors can be controlled by optimal shape design of the yoke, including holes and notches.

On the right-hand side of Figure 1.8, an alternative twin-aperture magnet design is shown [31]. This construction allows for easier winding of the coil ends, as the coil blocks in the two apertures form a common coil with a minimum bending radius of half of the beam separation distance (97 mm). Disadvantages are the high iron saturation in the horizontal median plane and consequently a higher dependence of the field quality on the excitation level, as well as a strong crosstalk between the apertures. Summing up, we list the differences between normal-conducting and superconducting accelerator magnets.

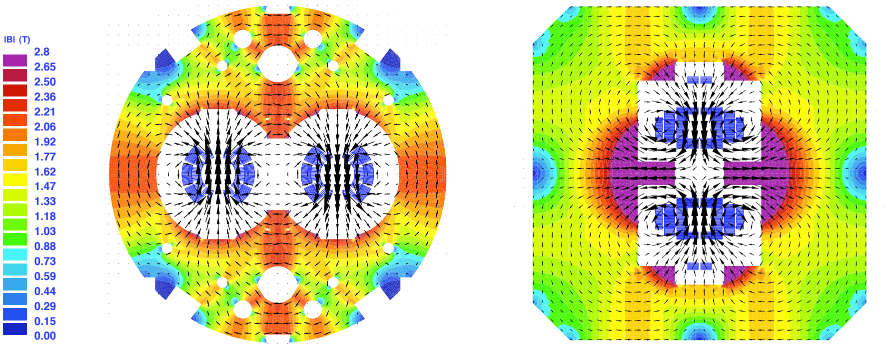

Figure 1.8 Left: Two-in-one LHC dipole with two coils in a common mechanical structure and iron yoke ($N \cdot I = 2{\cdot}944$ kA, $B_\mathrm{t} = 8.32$ T, $B_\mathrm{s} = 7.44$ T). Aperture diameter 56 mm. Right: Alternative design [31] with two apertures in a common coil design ($N \cdot I = 2 \cdot 1034$ kA, $B_\mathrm{t} = 8.34$ T, $B_\mathrm{s} = 7.35$ T). Aperture diameter 50 mm.

Normal-conducting magnets:

- The magnetic field is defined by the iron pole shape and limited to about 1.5 T. The conceptual design can be accomplished using one-dimensional field computation as described in Chapter 7.
- Normal-conducting magnets feature very high field quality because the yoke can be shaped with high precision. In addition, the field quality can be optimized by pole shims. Commercial finite-element software can be applied to the design as a “black box.”
- Conductor placement is not critical, although the stray field can be reduced by bringing the coil close to the air gap.
- Ohmic losses in the coils (16 MW for all LEP dipoles) require water cooling, resulting in high operational costs.
- The voltage drop across the ohmic resistance must be considered, particularly in view of a series connection of a string of magnets.
- Electrical interconnections in strings of magnets are easy to make and to check.
- Hysteresis effects in the iron yoke must be modeled.

Superconducting magnets:

- The field is defined by the coil layout, which requires accurate coil modeling and adapted computational tools for optimization of the field quality.

- The shaping of the coils in the end region requires special attention to limit performance degradation. In addition, the effective magnetic length is shorter than the physical length.
- The high current density in the superconductor allows the building, on an industrial scale, of accelerator magnets with a maximum field of 9 T using Nb–Ti composite wire.
- The contribution of the magnetization in the iron yoke to the main field in the aperture is limited to 30%. Thus nonlinear variations in the field quality due to inhomogeneous saturation of the yoke can be limited for a wide range of excitation levels.
- The enormous electromagnetic forces ($4\ \mathrm{MN\,m^{-1}}$ in the LHC main dipole at nominal excitation) require a careful mechanical design with adequate force-retaining structures.
- The voltage drop across the magnet terminals is limited to the inductive voltage during the ramping of the magnets.

A superconducting magnet system poses additional technological challenges in the domain of cooling and magnet protection:

- Operational stability must be guaranteed with heat transfer to the coolant, cryogenic installations (refrigerators), helium distribution lines, and insulation cryostats. Special designs for current feedthroughs from the room-temperature environment into the helium bath are required.
- Electrical interconnections of superconducting busbars are located inside the helium enclosure and cryostat and therefore impossible to verify once the accelerator is in operation.
- Protection against overheating during a resistive transition (quench) is required. This includes quench detection electronics, an energy extraction system with protection resistor, quench-back heaters, and cold bypass diodes, among other measures.
- Superconducting filament magnetization results in hysteresis effects and relatively large multipole field errors at injection field level. Magnetization-induced field errors are the principal reason for the installation of the spool-piece corrector magnets.

It is customary to refer to normal-conducting and superferric magnets as *iron-dominated* and superconducting magnets as *coil-dominated*. The latter can further be grouped into two classes [34]:

- Class 1 magnets for plasma confinement in fusion reactors, physics experiments, and magnetic energy storage (SMES), constructed for a field level of 4–5 T, and with large apertures in the range of meters. Owing to the magnet size and the large electromagnetic forces, the most challenging design aspect is the mechanical integrity.

- Class 2 magnets feature a high field and high current density but a relatively small aperture in the range of centimeters. Applications are nuclear magnetic resonance (NMR), magnetic resonance imaging (MRI), particle accelerators, superconducting motors and generators, magnetic separation, magnetic levitation, and high magnetic field research, among others. Critical issues are cable design, stability, magnet protection, and cooling.

1.3
Superconductor Technology

All superconducting synchrotron projects since the Tevatron at FNAL employ niobium–titanium (Nb–Ti) superconductors operated at cryogenic temperatures at or below 4.5 K. The advantage of the Nb–Ti alloy is the combination of good superconducting properties with favorable mechanical (ductility, tensile strength) and metallurgical properties that allow the coprocessing with different substrate materials such as copper and copper–nickel. Thus wires can be produced with the fine filaments necessary to control the field quality and to limit hysteresis losses in the magnets.

Even with Nb–Ti superconductors, the only way to obtain the required central field in the LHC main magnets is to apply cooling with superfluid helium II, a technology proven on a large scale with the Tore Supra Tokamak [8] built for fusion research at CEA (France).

After a worldwide industrial qualification program in the years 1994–1996, about 1300 tons of wire, extruded from more than 6000 billets, was produced and cabled to a total length of 7500 km.

1.3.1
Critical Current Density of Superconductors

The production of a Nb–Ti wire is nowadays achieved with a high homogeneity in the critical current density, above 1600 A mm^{-2} at 1.9 K in a 10 T applied field. Figure 1.9 shows the critical current density J_c of Nb–Ti as a function of the flux density B and temperature T. A magnet's working point on the load line is determined by the maximum flux and current densities in the coil for a given uniform temperature. The distance between the working point and the *critical surface* $J_c(B, T)$ along the load line determines the operational margin to *quench*.[14]

---

[14] A quench is the transition between the superconducting and the resistive state of the material. The critical surface modeling is presented in Section 16.2. Quench simulation and magnet-protection schemes are discussed in Chapter 18.

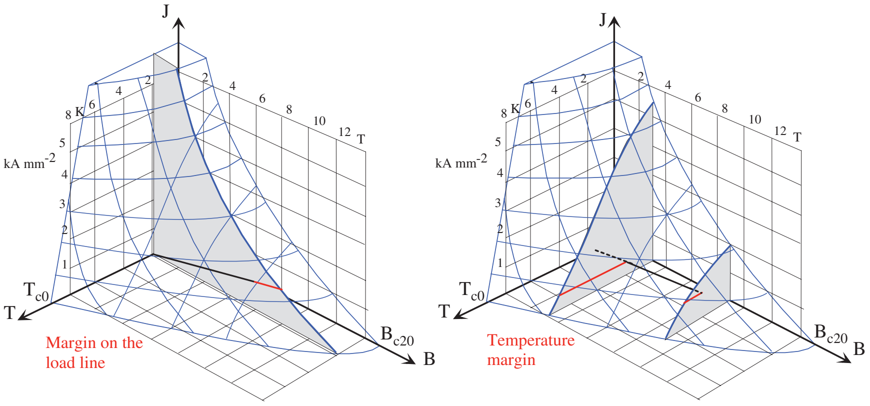

Figure 1.9 Critical surface of the Nb–Ti superconductor. Left: Operational margin of the magnet on the load line. Right: Temperature margin at a given field and current density.

Figure 1.9 (right) shows the temperature margin for a given flux density and current density. This temperature margin is important for the stable operation of the magnets at a given beam energy and intensity because of unavoidable beam losses and heat in-leaks through the magnet's cryostat.

Fields in excess of 14 T can, potentially, be achieved with accelerator-type magnets constructed with niobium–tin composite conductors. At the early stage of the LHC R&D phase, a mirror dipole magnet for operation at 4.5 K was constructed with Nb_3Sn conductors and reached a record value of 10 T [3]. Nevertheless, the Nb_3Sn magnet program was abandoned in 1991 due to the brittle nature of the material and because the stress-dependent critical current density results in performance degradation after coil winding. Furthermore, the minimum attainable filament sizes for this material are even nowadays too large to match the requirements of the LHC machine.[15] Conductors made of Nb_3Sn also require heat treatment, in which the niobium and tin react at a temperature of 700 °C to form the superconducting A15 phase of Nb_3Sn. The heat treatment can be performed before or after the coil winding; the two techniques are therefore known as react-and-wind and wind-and-react. While R&D is currently focused at the stress dependence of the material, short model magnets have achieved flux densities on the order of 14 T. Possible applications are magnets for the luminosity upgrade of the LHC and for next-generation hadron colliders. As a result of these efforts, the critical current density has doubled since the early 1990s, and record values for a single wire are as high as 3000 $\mathrm{A\,mm^{-2}}$ at 4.2 K and a 12 T applied field [24]. A good overview of magnet development using Nb_3Sn conductors is given in [32].

---

[15] Smallest diameter of 25 μm for modern powder-in-tube wires [24].

High-temperature superconductor (multifilamentary BSCCO[16] 2223 tape stabilized with a silver gold alloy matrix) is used in the LHC project for the current leads that provide the transition from the room-temperature power cables to the superconducting busbars in the continuous cryostat. A total of 1030 leads, for current ratings between 600 A and 13 kA [10], are mounted in electrical feed boxes. Each lead is made of a section of high-temperature superconductor (HTS) material, operating between 4.5 and 50 K in the vapor generated by heat conduction, and a normal-conducting copper part operating between 50 K and ambient temperature. By using HTS current leads, the heat influx to the helium bath can be reduced by a factor of 10 with respect to normal-conducting copper leads. In total, 31 km of BSCCO 2223 tapes were vacuum soldered at CERN to form more than 10 000 stacks, containing four to nine tapes depending on the current rating [11].

For use in high-field magnets, however, the critical current density of $300\,\mathrm{A\,mm^{-2}}$ at 8 T and 4 K would be too low and the material too brittle and too expensive. More information on critical currents obtained in technical superconductors can be found in [48].

For the parametric representation of the critical surface of Nb–Ti we use the empirical relation [14]

$$J_\mathrm{c}(B,T) = \frac{J_\mathrm{c}^\mathrm{ref} C_0 B^{\alpha-1}}{(B_\mathrm{c2})^\alpha}(1-b)^\beta \left(1-t^{1.7}\right)^\gamma , \tag{1.6}$$

with the fit parameters α, β, γ, and the normalized temperature t and normalized field b defined by $t := T/T_\mathrm{c0}$ and $b := B/B_\mathrm{c2}(T)$. The critical field is scaled with $B_\mathrm{c2} = B_\mathrm{c20}\left(1-t^{1.7}\right)$, where B_c20 is the upper critical field at zero temperature. For the calculation of the margin on the load line, as well as the temperature margin with respect to heat deposits due to beam losses, we use the following parameters [14]: The reference value for the critical current density at 4.2 K and 5 T is $J_\mathrm{c}^\mathrm{ref} = 3000\ \mathrm{A\,mm^{-2}}$, the upper critical field at zero temperature $B_\mathrm{c20} = 14.5$ T, the critical temperature at zero flux density $T_\mathrm{c0} = 9.2$ K, and the normalization constant $C_0 = 27.04$ T. The fit parameters are $\alpha = 0.57$, $\beta = 0.9$, and $\gamma = 2.32$. The maximum local error of the fit is in the range of 11% at low field and up to 5% at high field. It must be noted that critical current density values at a low field are determined from magnetization measurements and data at field levels above 3 T from I_c measurements of the strands. We will return to this point in Chapter 16.

Figure 1.10 (left) shows the critical current density of Nb–Ti at 1.9 K as a function of the applied field, together with the linear approximations

$$J_\mathrm{c}(B) = J_\mathrm{ref} + c\,(B_\mathrm{ref} - B) \tag{1.7}$$

---

[16] Bismuth strontium calcium copper oxide $Bi_2Sr_2Ca_2Cu_3O_{10}$ with $T_\mathrm{c} =$ 107 K, discovered in 1988.

around the reference points for both cable types. The slopes are given by

$$c := -\left.\frac{\mathrm{d}J_\mathrm{c}}{\mathrm{d}B}\right|_{B_\mathrm{ref}}, \tag{1.8}$$

and are in the range of 500 to 600 $\mathrm{A\,mm^{-2}\,T^{-1}}$. Figure 1.10 (left) also shows the load line of the LHC main dipoles. Nonlinearities due to iron saturation are disregarded. Note that the quench current of the magnet is limited by the critical current density in the coil, which is exposed to a 2–5% higher field than that of the magnet aperture. Important for the magnet performance is the engineering current density, J_E, which takes into account the copper matrix needed for stabilization, the filling factor of the cable, and the insulation thickness. Figure 1.10 (right) shows the temperature margin of the cables in the different coil blocks of the dipole magnet. The lines are the projections of the critical surface at a given flux density B onto the JT-plane; compare Figure 1.10 (right).

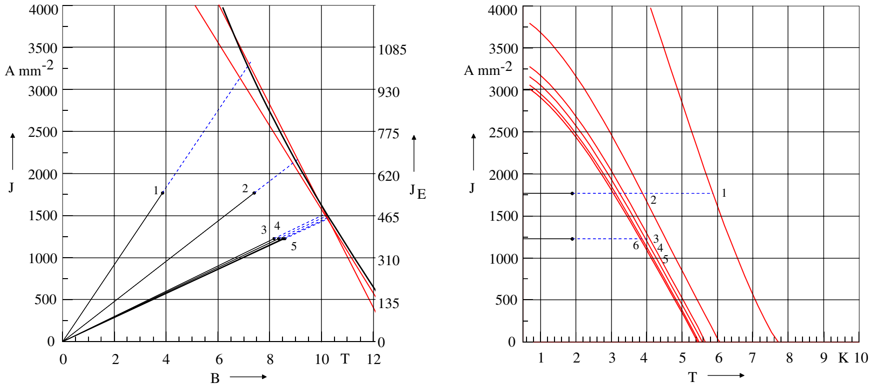

Figure 1.10 Left: Critical current density of Nb–Ti at 1.9 K as a function of the applied field (for linear approximations around reference points), together with the load line of the LHC main dipoles. Right: Temperature margin of the cables in the different coil blocks of the dipole magnet.

1.3.2
Strands

The *strands*[17] are made of thousands of Nb–Ti filaments embedded in a copper matrix that serves to stabilize the wire and to carry the current in the event of a quench, since superconductors have a high resistivity in the normal state.

---

[17] This is common parlance for superconducting wires; the terms are used synonymously.

A microphotograph of a strand and its filaments is shown in Figure 1.11. The filaments are made as small as possible (constrained by the manufacturing costs and interfilament coupling effects) in order to reduce remanent magnetization effects and to increase the stability against flux jumps during excitation, that is, the release of fluxoids from their pinning centers.[18]

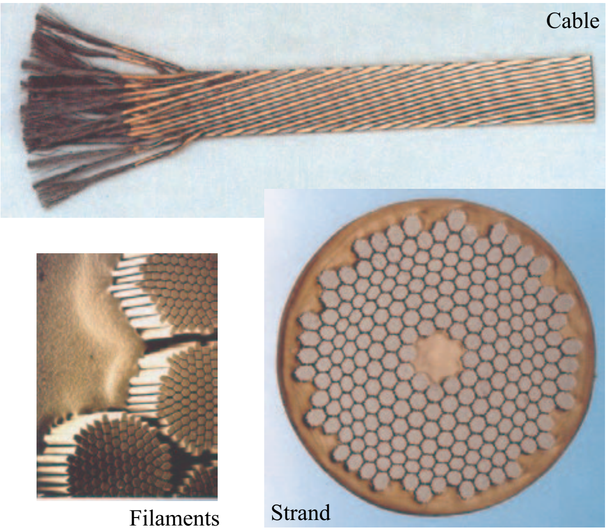

Figure 1.11 Cable for the inner layer of the LHC main dipole coils; microphotograph of the strand cross section and the superconducting filaments. Shown is a prototype wire produced with a double-stacking process.

The critical current density and the slope of the critical surface at the reference point (constant temperature of 1.9 K) are given for the strands used in LHC cables in Table 1.2. The critical current densities were measured for strands extracted from the cables, and therefore the degradation due to the cabling process is taken into account. Note that the values are scaled with the copper-to-superconductor area ratio, and are thus valid for the superconducting material only.

The critical current density of the superconductors (Figure 1.12) can be scaled with the strand filling factors

$$\lambda_{\mathrm{SC}} = \frac{1}{1+\eta}, \qquad \lambda_{\mathrm{Cu}} = \frac{\eta}{1+\eta}. \tag{1.9}$$

The quotient $\eta := a_{\mathrm{Cu}}/a_{\mathrm{SC}}$ is the area ratio of the copper cross section of the strand to the total superconducting filament cross section. The cross-sectional

---

[18] The remanent magnetization effects are proportional to the critical current density and the filament size, as is explained in Chapter 16.

Table 1.2 Characteristic data for the strands used in the main dipole (MB) cables, the MQM and the MQY quadrupole cables, and in the auxiliary busbar cable (Line N)[a].

Magnet	Strand 1 MB inner	Strand 2 MB outer	Strand 5 MQM	Strand 6 MQY	Line N
Diameter of strands (mm)	1.065	0.825	0.48	0.735	1.6
Strand pitch length (mm)	25	25	15	15	25
Copper to SC area ratio	1.65	1.95	1.75	1.25	> 9
Filament diameter (μm)	7	6	6	6	58
Number of filaments/strand	8900	6500	2300	6580	17
T_{ref} (K)	1.9	1.9	1.9	4.5	4.2
B_{ref} (T)	10	9	8	5	1
$J_c(B_{\mathrm{ref}}, T_{\mathrm{ref}})$ $(\mathrm{A\,mm^{-2}})$	1433.3	1953.0	2872	2810	> 5000
$-\mathrm{d}J_c/\mathrm{d}B$ $(\mathrm{A\,mm^{-2}\,T})$	500.34	550.03	600	606	n.s.
$\rho(293\ \mathrm{K})/\rho(4.2\ \mathrm{K})$ of Cu	> 70	> 70	80	80	> 100

[a] The Line N cable is made from the same highly stabilized strands that are used in MRI magnets. The cable is used to power the lattice corrector magnets mounted in the short straight section. n.s. = not specified.

area of diffusion barriers and the strand coating is therefore disregarded. The copper-to-superconductor area ratio η is 1.65 for the inner-layer dipole cable, and 1.95 for the outer-layer dipole cable, which was also used for the production of the main quadrupoles.

In the case of Nb_3Sn composite conductors, with filaments including an inner core, the composition is more complex and one often refers to the ratio of copper to noncopper areas.[19] The brittleness of the material prevents it from being extruded from ingots. Instead, a diffusion technique is applied, where the elements of the compound are reacted at 700 °C for several hours. The reaction is performed after wire production or after the coil winding only. The ratio of copper to noncopper areas depends on the various production techniques, such as the most common bronze (Cu–Sn) diffusion technique, the external tin diffusion technique, and the powder-in-tube (PIT) process [26,28].

The manufacturing of multifilamentary Nb–Ti composite wires is accomplished by stacking hexagonal rods of Nb–Ti inside a sealed copper canister, an assembly usually referred to as a billet. Practical limitations are minimum rod diameters of approximately 1.5 mm and a maximum number of rods of 15 000. The billet is then hot-extruded, followed by conventional wire drawing in multiple stages to reach the final diameter. After the drawing process, the wire is annealed at 400 °C to form the dislocation cell structures needed for flux pinning and thus for enhancing the critical current. The filament size chosen for the LHC (7 μm for the strand in the inner-layer cable and 6 μm in the

[19] Consequently, the noncopper critical current density J_c is the relevant quantity for magnet design.

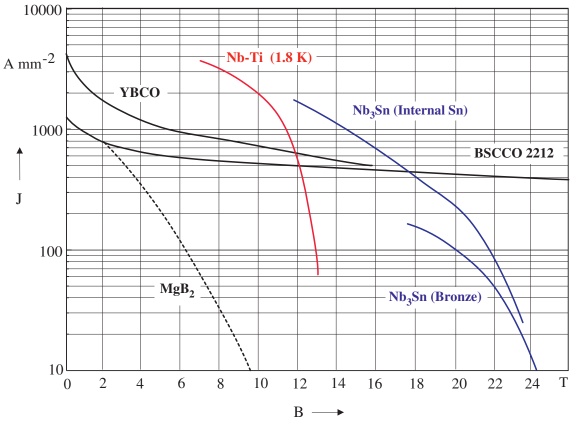

Figure 1.12 Critical current density of superconductors (at 4.2 K if not otherwise stated); source [48].

outer-layer cable) allows the fabrication of the wires in a single-stacking process. Even finer filaments can be obtained by a double-stacking process, where rods with a hexagonal section, resulting from a first extrusion, are stacked into a secondary billet, which is then extruded again and drawn to the final wire diameter. The filament pattern for a wire produced with the double-stacking process is shown in Figure 1.11.

Due to the extrusion and drawing process, the filament can deviate from the optimum round shape. The distortions may also vary along the length of the wire, a deformation usually referred to as *sausaging*. Distorted filaments show higher hysteresis losses and a wider resistive transition, resulting in an effective resistivity according to the empirical law

$$\rho = \frac{E_c}{J_c}\left(\frac{J}{J_c}\right)^{n-1}. \tag{1.10}$$

The factor n, called the *resistive transition index*, can be seen as a quality factor of the production. The field-dependent resistive transition index obtained for the LHC wire production is $n = 42$ at 10 T and $n = 48$ at 8 T [53].

1.3.3
Cables

According to Eq. (1.5) the trajectory radius of the particle increases with its momentum. As both the flux density and the aperture of the bending magnets are limited, the magnetic field must be ramped synchronously with the particle energy. The LHC main dipole magnets are ramped from the injection field level of 0.54 T to their nominal field of 8.33 T, according to the excitation

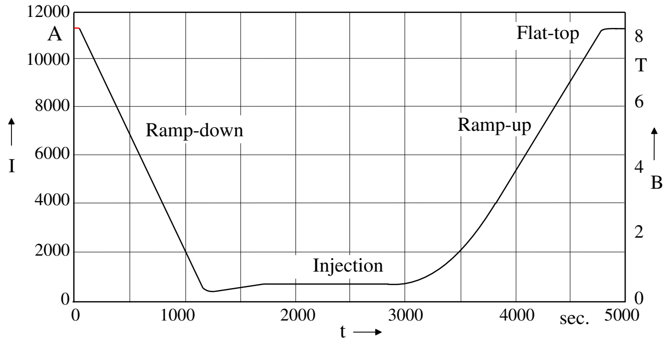

Figure 1.13 Excitation cycle [19] for the LHC main dipole circuits.

cycle shown in Figure 1.13. The mathematical description of the excitation cycle is given in Appendix C.

To ensure good tracking of the field with respect to the current and to reduce the number of power converters and current feedthroughs, the magnets in superconducting synchrotron accelerators are connected in series. Disregarding nonlinearities due to iron saturation in the magnet yokes, and the stored energy at an injection field level, the induced voltage during the ramping of an LHC magnet string is approximately

$$U \approx \frac{2E}{It}, \tag{1.11}$$

where E is the stored energy in the string of 154 dipoles at nominal current, t is the current rise time of 1200 s, and I is the nominal operating current of 11 800 A. The maximum voltage in the power supplies of the main dipole circuit can be calculated for a stored energy of 1.1×10^9 J (approximately 300 kW h) to 155 V. To avoid higher voltages, the coils of the LHC dipole and quadrupole magnets are wound from so-called *Rutherford cables* of trapezoidal shape. The cabling scheme is identical to the Roebel[20] bar known in the domain of electrical machines; see Figure 1.14.

It was shown in the Rutherford laboratory in the early 1970s that the cable could be produced, without wire or filament breakage at the cable edges, by rolling a hollow, twisted tube of wires. Two layers of fully transposed strands limit nonuniformities in the current distribution within the cable caused by the cable's self-field and flux linkage between the strands.[21] The Roebel scheme allows cable compaction of 88–94% without strand damage and good control of the dimensional accuracy on the order of 0.01 mm. The cable used

[20] Ludwig Roebel (1878–1934), patent 1912.

[21] Note that the strands in twisted litz wire are not fully transposed, as strands positioned in the center always remain there.

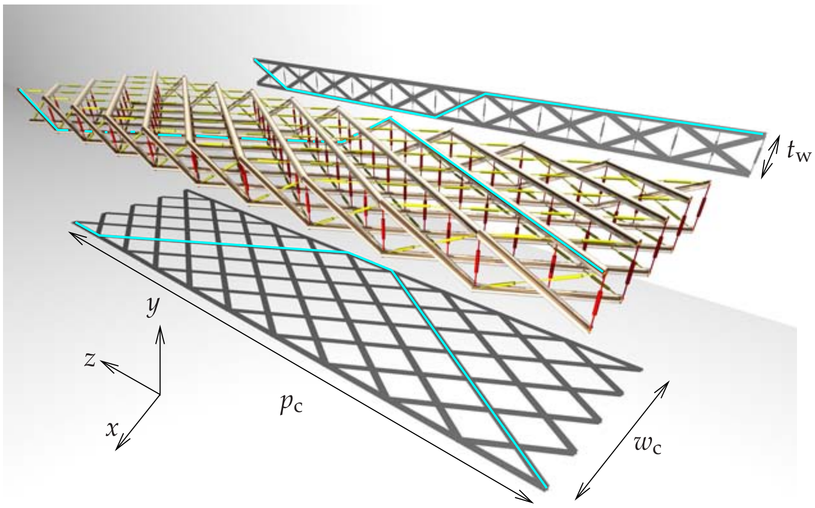

Figure 1.14 Winding scheme of a Rutherford cable (schematics with 10 strands). The blue path shows the full transposition of a superconducting strand. Depending on the transposition pitch and the cable compaction, the uninsulated strands are in contact, which gives rise to cross resistances (red) and adjacent resistances (yellow).

for the inner layer of the LHC main dipole coil contains 28 superconducting strands, while the cable used in the outer-layer dipole coil and in the main quadrupoles contains 36 strands.

For magnet design it is desirable that the cable be *keystoned*[22] at an angle that allows the winding of perfect arc segments. However, due to the critical current degradation during cabling, the keystone angle is limited; see Figure 8.1 for a cross-sectional view of a block of cables in the inner layer of the LHC main dipole coils. In [54] the packing factor at the cable's narrow edge is defined by

$$\lambda_\mathrm{n} := \frac{a_\mathrm{s}}{0.5\, t_\mathrm{n} d_\mathrm{s}} = \frac{\pi d_\mathrm{s}}{2 t_\mathrm{n}} \tag{1.12}$$

where a_s is the strand cross-sectional area, t_n is the cable thickness at its narrow edge, and d_s is the strand diameter. Measurements have revealed that the amount of degradation increases considerably for narrow-edge packing factors exceeding 0.98 because of local reduction in the strand cross section and breakage of filaments during cabling.[23] The narrow-edge packing factor for

---

[22] A keystone is an architectural piece at the apex of an arch, of trapezoidal shape, locking the other stones into position.

[23] In $\mathrm{Nb_3Sn}$ strands, breakage of antidiffusion barriers can lead to incomplete filament reaction [23].

Table 1.3 Cable characteristic data for inner-layer (IL) and outer-layer (OL) main dipole (MB) coils[a].

Magnet	Cable 1 MB (IL)	Cable 2 MB (OL)	Cable 4 MQM	Cable 5 MQY (OL)	Cable 6 MQY (IL)
Strand	1	2	5	5	6
Bare width (mm)	15.1	15.1	8.8	8.3	8.3
Bare thickness, thin edge (mm)	1.736	1.362	0.77	0.78	1.15
Bare thickness, thick edge (mm)	2.064	1.598	0.91	0.91	1.40
Mid thickness (mm)	1.9	1.48	0.84	0.845	1.275
Cable cross section (mm^2)	28.69	22.35	7.39	7.014	10.58
Keystone angle (degree)	1.25	0.9	0.91	0.89	1.72
Aspect ratio	7.95	10.2	10.47	9.82	6.51
Insulation narrow side (mm)	0.150	0.150	0.08	0.08	0.08
Insulation broad side (mm)	0.120	0.130	0.08	0.08	0.08
Insul. cable cross sec. (mm^2)	32.96	27.0	8.96	8.50	12.14
Cable transp. pitch length (mm)	115	100	66	66	66
Number of strands	28	36	36	34	22
Cross section of Cu (mm^2)	15.3	12.6	4.1	3.9	5.2
Cross section of SC (mm^2)	9.6	6.6	2.4	2.2	4.1
SC filling factor λ_{tot}	0.29	0.24	0.27	0.26	0.34

[a] Cable 3 for the main quadrupole (MQ) coil is identical with cable 2. Cables 5 and 6 are used for the insertion quadrupoles MQM and MQY.

cable 1 used in the LHC main dipoles is 96%. The cable thickness at its wide edge is chosen in such a way that the upper and the lower strands are in contact in order to maintain cable integrity during coil winding [54]. The cable packing factor is defined as the ratio of the bare strand volume to the cable volume,

$$\lambda_{\text{c}} := \frac{n\pi d_{\text{s}}^2}{2w_{\text{c}}(t_{\text{n}} + t_{\text{w}})\cos\psi}, \tag{1.13}$$

where w_{c} is the cable width, t_{w} is the cable thickness at its wide edge, and ψ is the pitch angle. The pitch angle can be calculated from

$$\tan\psi = \frac{2w_{\text{c}}}{p_{\text{c}}}, \tag{1.14}$$

where p_{c} is the length of the transposition pitch.

For the 2D calculations we set $\cos\psi = 1$ in Eq. (1.13). Furthermore, we define λ_{i} as the quotient of the insulated cable cross section and the bare cable cross section. The engineering current density can therefore be calculated from

$$J_{\text{E}} = \lambda_{\text{f}}\,\lambda_{\text{c}}\,\lambda_{\text{i}} J_{\text{c}} =: \lambda_{\text{tot}} J_{\text{c}}\,. \tag{1.15}$$

The total superconductor filling factor λ_{tot} is in the range of 30%. The values for the LHC cables are given in Table 1.3. Due to field variations in the coil ends and resistance differences in the solder joints between coils, the current may not be equally distributed within the Rutherford cable. For this reason the individual strands are not insulated. This gives rise to adjacent and transverse (cross) electrical contact resistances between the strands; see Figure 1.14. Across these resistances closed loops are formed in which coupling currents can be induced during the ramping of the magnets, as well as during the fast discharge in the event of a quench. While in the first case these coupling currents produce unwanted field distortions, in the latter case they help to distribute the stored magnetic energy evenly by inductive heating of the coil, a process known as *quench-back*.

The losses can be calculated by an electrical network model discussed in Chapter 17. They scale quadratically with the magnetic flux density, the transposition pitch, and the cable width and are inversely proportional to the electrical contact resistance[24] and the cable thickness [70]. In order to impose tight control over the contact resistance for the series production of the magnets, a silver tin coating on the strands guarantees a cross-contact resistance on the order of some tens of μΩ, a good compromise in terms of ramp-induced field errors, stability, and quench-back.

In the case of the main dipole, the cable is insulated with three layers of polyimide film. Two layers (in total 50.8 μm thick) are wrapped on the cable with a 50% overlap, and another, 68.8 μm thick, is wrapped around the cable with a spacing of 2 mm, and insulation scheme sometimes referred to as a barber-pole wrapping. An adhesive layer with a nominal thickness of 5 μm is applied to the outside of the barber-pole wrapping in order not to bond the insulation to the cable and thus avoid quenches due to energy release by bond failure. The insulation protects the cable from a turn-to-turn voltage of 50 V at quench, yet it has sufficient porosity and percolation for helium cooling. The main parameters of cable used in LHC magnets are given in Table 1.3.

Magnet cooling with superfluid helium at 1.8 K benefits from the very low viscosity and high thermal conductivity of the coolant. However, the heat capacity of the superconducting cables is reduced by nearly an order of magnitude compared to an operation at 4.5 K. This results in a higher temperature rise for a given deposit of energy. To avoid quenching below the so-called *short-sample limit*, all movement of the coil must be prevented by the use of an appropriate force-retaining structure. Because the forces and stored energy in the magnets increase with the square of the magnetic flux density, the mechanical design required an extensive R&D phase carried out at CERN during the years 1988 to 2001, in close collaboration with other HEP Institutes and with European industry.

---

[24] The contact resistances are defined as the lumped element resistances in the network model; see Figure 1.14.

1.4
The LHC Dipole Coldmass

The coil-winding direction is defined by the first cable on the center-post when looking down on the winding mandrel (counter-clockwise for the inner-layer dipole coils, clockwise for the outer-layer coils). Experience has shown that best winding results are obtained if left-hand lay cables are wound in clockwise direction, while right-hand[25] lay cables are wound in counter-clockwise direction [52]. It is advantageous for making internal cable joints that the cables in the two coil layers have opposite pitch direction. Nevertheless, all Rutherford cables used in the LHC project are left-hand lay cables; see Figure 1.11.

As the field distribution is extremely sensitive to coil-positioning errors, each coil is polymerized after winding. The press and heating system of the mold allows the coil to be cured for 30 min at 190 °C under a maximum pressure of 80–90 MPa. This process activates the adhesive layer on the insulation to glue the turns together. In this way, the mechanical dimensions of the coils can be controlled within a tolerance of ±0.05 mm. The size and elastic modulus of each coil are then measured to determine the pole and coil-head shimming for the collaring procedure. The outer-layer coil is fitted onto the inner with a fiberglass-reinforced ULTEM® spacer between the two layers. The spacer gives a precise mechanical support for the outer-layer coil and it is slotted in order to provide channels for the superfluid helium. Because of its appearance, this spacer is also referred to as the *fishbone*.

The four coil packs for the twin-aperture magnet are assembled in a mechanical force-restraining structure, known as *collars*, made of preassembled packs of 3-mm-thick austenitic steel laminations (Nippon Steel YUS 130S) with a relative permeability of less than 1.003. A 3D rendering of the collar packs is shown in Figure 1.16. The required pole-shim thickness is calculated such that the compression under the collaring press is 120 MPa. After the locking rods are inserted into the collar stack and external pressure is released, the residual coil prestress is 50–60 MPa on both layers.

The collared coils are surrounded by an iron yoke, which not only enhances the magnetic field but also reduces the stored energy and shields the stray field. The stacking factor of the 5.8-mm-thick yoke laminations is 0.985 and thus provides for a helium buffer. The yoke also allows for sufficient helium flow in the magnet's axial direction and sufficient cross section for transverse heat conduction to the heat exchanger tube. The yoke laminations are made of low-carbon mild steel, hot-rolled and annealed, and precision punched with a tolerance of ±0.05 mm. The laminations are preassembled in 1.5-m-long

---

[25] Left-hand lay cables (seen as the strand moves away from the viewpoint) are also said to have s-pitch; right-hand lay cables to have z-pitch.

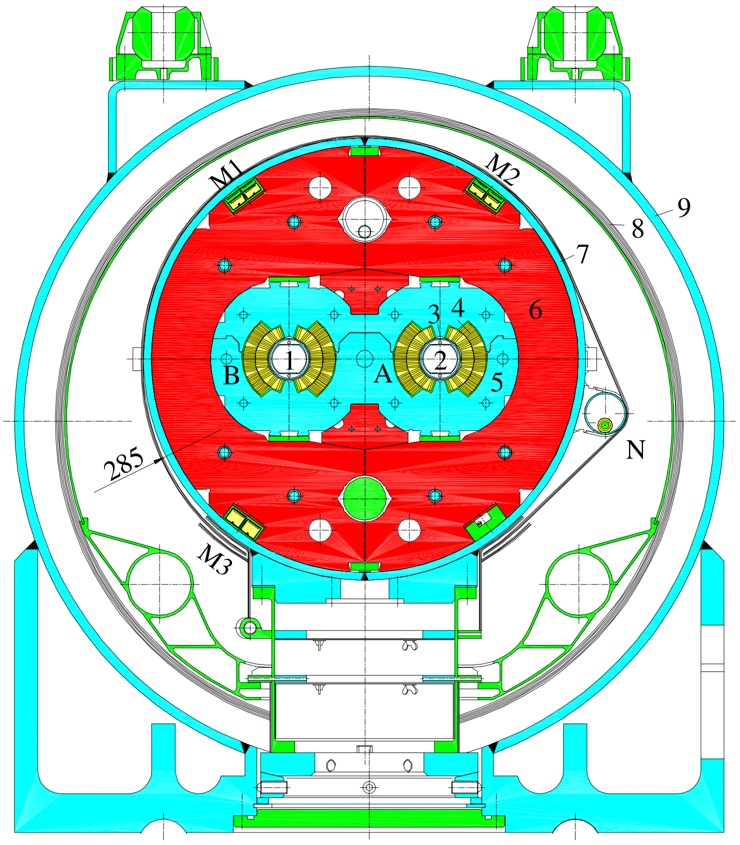

Figure 1.15 Cross section of an LHC cryodipole prototype. 1: Aperture 1 (outer ring). 2: Aperture 2 (inner ring). 3: Cold-bore and beam screen. 4: Superconducting coil. 5: Austenitic steel collar. 6: Iron yoke. 7: Shrinking cylinder. 8: Super-insulation, 9: Vacuum vessel. M1–M3: Busbars for the powering of the main dipole and quadrupole circuits. N: Auxiliary busbar for the powering of arc-corrector magnets.

packs, which are mounted into half-yokes. The collared coils, yoke, and busbars are enclosed in an austenitic steel pressure vessel, which acts as a helium enclosure. This construction forms the dipole coldmass shown in Figure 1.15, a containment filled with static, pressurized superfluid helium at 1.9 K. The principal components of the helium vessel are the main cylinder, composed of two half-shells, and the end covers. The half-shells are fused in a dedicated welding press designed to yield a circumferential stress of around 150 MPa at ambient temperature.

The aperture of the bending magnet must be large enough to contain the *sagitta* of the proton beam, or the magnet must be curved accordingly. To ob-

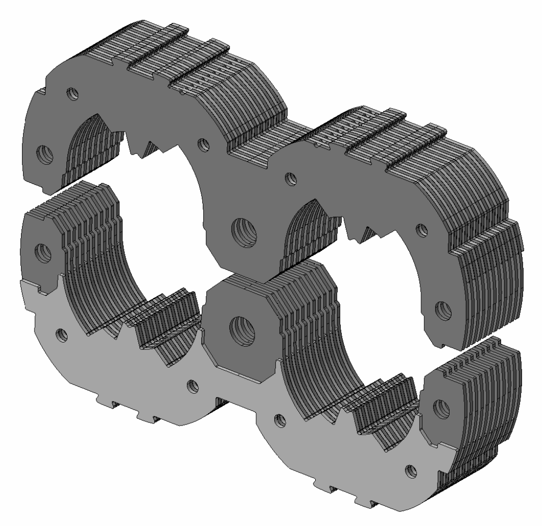

Figure 1.16 3D rendering of the collar packs for the LHC main dipole [56].

tain the nominal sagitta of 9.14 mm, the helium vessel is curved to 12 mm in the welding press in order to account for the spring-back after the coldmass is released from the press. After the assembly of the half-yokes and the welding of the helium vessel, the gap between the half-yokes is closed. The prestress has been chosen such that the gap between the half-yokes remains closed during cool-down and excitation of the magnet.

1.5
Superfluid Helium Physics and Cryogenic Engineering

In order to operate a superconducting magnet, the cooling agent must have a temperature well below the critical temperature of the superconductor. For Nb–Ti the critical temperature at zero flux density is 9.2 K and for Nb_3Sn it is 18.1 K.

Helium has the distinction of having no triple point; it solidifies only at pressures above 2.5 MPa, even at absolute zero. In addition, there are two liquid phases as indicated in Figure 1.17. Liquid ^{4}He below its lambda line, in a state called *helium II*, exhibits unusual characteristics. The transition between the two liquid phases is accompanied by a large peak in the heat capacity, but no latent heat. The lambda point refers to the anomaly in the heat capacity at 2.17 K, an effect also seen at the transition temperature of superconductors. When helium II flows at low velocity through capillaries even in the µm-diameter range, it exhibits no measurable viscosity. This frictionless flow, or *superfluidity*, was discovered independently by Allen and Misener [1], and by Kapitza [37] in 1938. The phenomenon was later explained theoretically by London,[26] who suggested a connection to Bose–Einstein[27] condensation, and by Tisza[28] who described a two-fluid model with condensed and non-condensed atoms being identified with the superfluid and the normal state, respectively. In 1941 Landau[29] suggested that the superfluid state can be understood in terms of phonons and rotons [29]. Introductions to superfluid helium physics can be found in [64] and [61].

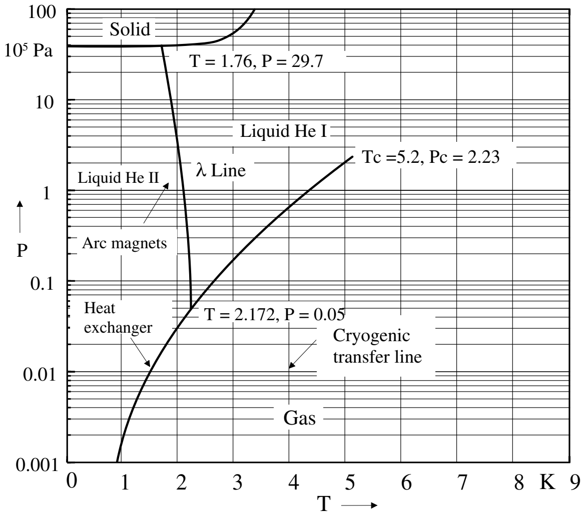

Figure 1.17 Phase diagram of ^{4}He and the thermodynamic states of the coolant in the LHC cryogenic system.

Superfluid helium has become a technical coolant subsequent to the work of Bon Mardion and others [49]. It is used in high-field magnets for condensed-matter research and nuclear magnetic resonance studies, and for magnetic confinement fusion in the Tore Supra Tokamak [8]. It also cools RF acceleration cavities in the CEBAF linear accelerator at the Jefferson Laboratory (USA) and the free electron laser, VUV-FEL at DESY.

The main reason for choosing superfluid helium as the coolant of the LHC magnets is the very low operating temperature, which increases the critical current density of the Nb–Ti superconductor. A disadvantage is the low specific heat capacity of the cable at superfluid helium temperature. This requires taking full advantage of the superfluid helium properties for thermal stabilization, heat extraction from the magnet windings, and heat transport to the

[26] Fritz London (1900–1954).
[27] Satyendra Nath Bose (1894–1974), Albert Einstein (1879–1955).
[28] László Tisza (1907–2009).
[29] Lew Landau (1908–1968).

cold source. With its low viscosity, superfluid helium can permeate the cables and buffer thermal transients, thanks to its high volumetric specific heat close to the lambda point, which is approximately 2000 times higher than that of the conductors. The excellent thermal conductivity of the fluid enables it to conduct heat without mass transport.[30]

In order to benefit from these unique properties, the electrical insulation of the cable must have sufficient porosity and percolation while preserving its mechanical resistance and dielectric strength [41]. These conflicting requirements are met by a multilayer wrapping of polyimide film with a partial overlap similar to the barber-pole wrapping described in Section 1.3.3.

As the thermal conductivity of superfluid helium remains finite, it is impossible to transport refrigeration power from one refrigerator across a 3.3-km-long LHC sector.[31] The LHC magnets operate in a static bath of pressurized superfluid helium close to atmospheric pressure at 0.13 MPa. Avoiding low-pressure operation in a large cryogenic system limits the risk of inward air leaks and helium contamination. In addition, saturated helium II exhibits low dielectric strength with the risk of electrical breakdowns at fairly low voltages.

The high-conductivity mono-phase liquid in the coldmasses is continuously cooled by heat exchange with saturated two-phase helium, flowing in a continuous heat exchanger tube. The deposited heat is absorbed quasi-isothermally by the latent heat of vaporization of the flowing helium. Advantages of this cooling scheme are the absence of convective flow in normal operation, the limited space it occupies in the magnet cross section, and the capacity to limit quench propagation between magnets in the string [42].

In view of the low saturation pressure of helium at 1.8 K, refrigeration by vapor compression requires a pressure ratio of 80 to bring the helium back to atmospheric pressure. To limit the volume-flow rate and hence the size of equipment, the large mass-flow rate in a high-power refrigerator must be processed at its highest density. This can only be done with contact-free, vane-free, nonlubricated (and therefore noncontaminating) cryogenic compressors. Hydrodynamic compressors of the axial-centrifugal type are used in multistage configurations. The LHC uses eight 1.8 K refrigeration units, each with a refrigeration power of 2.4 kW, based on multistage axial-centrifugal cryogenic compressors operating at high rotational speed on active magnetic bearings. This technology was developed in industry following CERN's specifications. The measured performance coefficient, that is, the ratio of electrical power to cooling power at 1.8 K is 950.

---

[30] The thermal conductivity of He II is more than three orders of magnitude higher than the thermal conductivity of water while its viscosity is four orders of magnitude lower than that of water.

[31] The thermal conductivity of superfluid helium is about 3000 times that of oxygen-free, high conductivity copper (OFHC) at room temperature.

The cryogenic system must cope with load variations during magnet ramping (ac losses in the cable) and stored-beam operation (synchrotron radiation, beam image currents, photoelectrons adsorbed by the beam screen, and random loss of particles, among others). The cryogenic system must also enable the cool-down of the magnet string in one sector in a maximum time of 15 days while avoiding thermal gradients exceeding 75 K per coldmass. In addition, the system must be able to handle the heat release during the resistive transition of magnets, by limiting the quench propagation to neighboring magnets and by containing the resulting pressure rise within the 2 MPa design pressure of the helium enclosure. Helium is discharged at high flow rate into a *header* with a large acceptance, which can thus act as a temporary storage, before it is discharged into 250 m^3 gas-storage vessels located at the surface areas of the LHC.

1.6
Cryostat Design and Cryogenic Temperature Levels

In view of the high thermodynamic cost of refrigeration at 1.8 K, the thermal design of the LHC cryogenic components aims at intercepting the largest fraction of applied heat loads at higher temperatures. The temperature levels are:

- 1.9 K for the quasi-isothermal superfluid helium for the magnet coldmass.
- 4 K at very low pressure in the cryogenic transfer line.
- 4.5 K normal saturated helium for cooling special superconducting magnets in the insertion regions and the superconducting accelerator cavities.
- 4.6–20 K for lower-temperature heat interception and for the cooling of the beam screens.
- 50–65 K for the thermal shields as first heat intercept level in the cryostat.
- 20–300 K for the cooling of the resistive section in the current leads.

The coldmass, weighing 28.5 tons, is assembled inside its cryostat, which comprises a support system, cryogenic piping, radiation insulation, and thermal shields, all contained within a vacuum vessel. The vacuum, at a pressure below 10^{-4} Pa, together with two thermal shields covered with super-insulation, minimizes inward heat conduction and radiation to the coldmass.

The cryostats combine several low-temperature insulation and heat intercept techniques, support posts made of fiberglass-epoxy composite for low thermal conductivity, low-impedance thermal contacts under vacuum for heat intercepts, and multilayer insulation blankets. The blankets, known as *super-insulation*, consist of alternating layers of highly reflective material and low-conductivity spacer material. The blankets are manufactured from sheets of

PET[32] film, coated with 40 μm aluminum on each side, and interleaved with polyester-net spacing sheets. The thermal shield, made of rolled high-purity aluminum, is equipped with two superimposed blankets of 15 layers each. The coldmasses and diode boxes are equipped with single blankets of 10 layers each.

1.7
Vacuum Technology

In general, vacuum conditions are obtained by removing gases from the contained volume by pumping (fast rotating turbo-molecular, and ion pumps) or by binding them via chemical or physical forces in the bulk of the pumping material (getters, sorption pumps) [39]. In the LHC straight sections that are at room temperature, the pressure requirements are fulfilled by ultra-high vacuum (UHV) technology with nonevaporable getter coatings (NEG), a technology developed at CERN [9].

The LHC has three distinct vacuum systems: The insulation vacuum systems for the continuous cryostat in the LHC arcs and the helium distribution line, and the beam vacuum system for the LHC arc and transfer lines for injection and beam dump. The insulation vacuum, covers a total volume of about 640 m^3; its room-temperature pressure need not be better than 10 Pa before cool-down. This is achieved with standard mechanical pumping groups. At cryogenic temperatures and in the absence of any significant air leak, the pressure will attain 10^{-4} Pa [44] by *cryosorption pumping* on the external surface of the magnet coldmasses. Vacuum separation in the nearly 3-km-long continuous arc-cryostat is achieved by vacuum barriers, such that the subsections can be individually commissioned, pumped, and leak tested.

The requirements for the beam vacuum are much more stringent. To ensure the required 100 h beam lifetime and a low background to the experimental areas, the equivalent hydrogen gas densities should remain below 10^{15} m^{-3} in the arc[33] and below 10^{13} m^{-3} in the interaction regions in order to minimize nuclear scattering of protons on the residual gas. Additional requirements result from magnet quench limits,[34] resistive power dissipation by beam image currents, beam-induced *multipacting*, beam loss by nuclear scattering, heat loads from beam gas scattering, and stimulated gas desorption from synchrotron radiation in the arcs.

[32] Polyethylene terephthalate.

[33] Corresponding to 7×10^{-8} Pa at 5 K.

[34] The beam pipes in the center of the superconducting magnets are in direct contact with the 1.9 K helium bath and very close to the inner-layer dipole coil.

In the LHC arc beam pipe, the pumping of hydrogen and all other gas species (except helium) relies on cryosorption pumping on the 1.9 K cold bore. Gases will be adsorbed by the attractive van der Waals[35] forces exerted by a cold surface, that is, when the energy of evaporation is less than the adsorption energy on the surface. Cryosorption is limited by the saturated vapor pressure of the gas at a given temperature. Below 20 K, only neon, hydrogen, and helium have a significant saturated vapor pressure and require special precautions, for example, avoiding helium leaks from the cryogenic distribution lines or the coldmasses themselves.

It is essential to limit heat flow to the 1.9 K circuit due to synchrotron radiation (0.2 $\mathrm{W\,m^{-1}}$), nuclear scattering of the high energy protons on the residual gas (0.1 $\mathrm{W\,m^{-1}}$), beam image currents (0.1 $\mathrm{W\,m^{-1}}$), and electron clouds (0.2 $\mathrm{W\,m^{-1}}$) [44]. There is a limit to cryosorption set by beam-induced energetic particles generating desorption of bound gas species, which increases the outgassing rate and hence the pressure in the vacuum system. In the LHC, with its synchrotron radiation of 10^{17} photons per meter second, this recycling effect of adsorbed gas dominates the wall-pumping of hydrogen to such an extent, that any directly exposed surface loses all useful pumping efficiency [30].

Thus a racetrack-shaped *beam screen*, actively cooled to temperatures between 5 and 20 K for nominal cryogenic conditions, is inserted into the cold bore of all magnets and connection cryostats. The beam screen, shown in Figure 1.18 (right), intercepts the power deposited by the synchrotron radiation at a higher temperature level. It also intercepts the power deposited by electron clouds during the conditioning phase and limits the condensed gas coverage on the surface exposed to the impact of energetic particles. The manufacturing process of the beam screen starts by colaminating a specially developed low-permeability austenitic steel strip with a 75-μm-thick copper sheet, followed by the punching of pumping slots covering 4% of the surface area. This is a compromise aimed at keeping the radio frequency losses low while limiting the reduction of the net pumping speed for hydrogen. Without the pumping slots, the surface of the screen would not provide sufficient pumping capacity, as the equilibrium vapor density at 5 K for a monolayer of hydrogen exceeds the acceptable limits by several orders of magnitude. The coated steel strip is then rolled into the final shape of the beam screen. The structure is closed with a longitudinal laser weld on one side. Particular care was taken in the composition of the austenitic steel in order to avoid ferrite formations during welding [58]. As the power dissipated by the beam image currents depends on the resistivity of the beam screen, the heat load is reduced by the copper layer, profiting from the fact that the resistivity of high-purity copper at cryogenic temperatures is reduced by a factor of 100 with respect to room temperature.

---

[35] Johannes Diderik van der Waals (1837–1923).

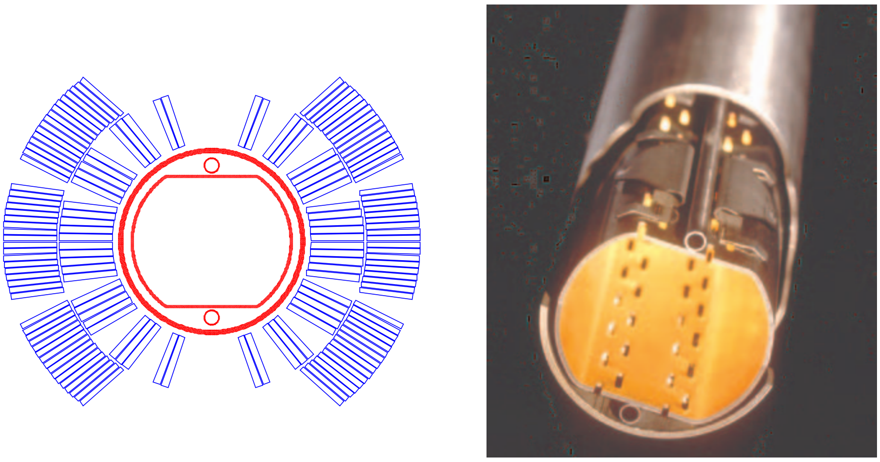

Figure 1.18 Left: Cross section of the LHC main dipole coil with the geometrical model of the cold bore and beam screen. Right: Photograph of the beam screen showing the pumping slots and the heat exchanger.

The beam screen is cooled by two austenitic steel heat-exchanger tubes, laser-welded onto the beam screen tube, allowing for an extraction of up to $1.13\,\mathrm{W\,m^{-1}}$ under nominal cryogenic conditions. The beam screen is fixed on the cold bore at one extremity of the cryomagnet. At the other extremity an expansion bellows is installed to allow for differential thermal expansion between the cold bore and the beam screen [44]. During ramping of the LHC machine, and in-particular when a quench occurs in the magnet, the beam screen is submitted to a horizontal expansion force due to the induced eddy currents.

We must also account for the effect of the beam screen on the field distribution in the magnet apertures; see Chapter 15. The model for the numerical field computation is shown in Figure 1.18 (left).

1.8
Powering and Electrical Quality Assurance

The magnet powering system for the LHC is complex. More than 10 000 magnet elements are connected in 1612 electrical circuit of 131 different types. The powering equipment includes:

- Current leads with HTS material for a 600–13 000 A current rating, as well as normal-conducting leads for a 60–120 A current rating.
- Electrical distribution feed-boxes to house the current leads.

- Superconducting power transmission lines in IPs 1, 3, and 5 of the LHC, where space constraints do not allow the installation of the electrical distribution feed-boxes close to the string of cryomagnets. The superconducting cables in these links are cooled by a flow of supercritical helium at 3.6×10^5 Pa and 4.5–6 K.
- Rigid busbars with thermal expansion loops for the 13 000 A main circuits, 120 km of multiwire cable for the corrector magnet circuits with a current rating of 600 A, and 600 A and 6 kA flexible busbar cables for the powering of the correctors in the short straight sections. The latter are routed in a separate cryogenic distribution line (line N) shown in Figure 1.15.
- Quench-protection equipment including quench protection electronics, quench-back heater power supplies, energy-extraction systems, high-current bypass diodes, and a supervision system.
- High-precision power converters for high currents (13 kA) at rather low voltages; 3–35 V in a steady state with peak voltages not exceeding 190 V.

Several tens of thousands of superconducting connections had to be made during the installation of the magnets in the LHC tunnel in the years 2005–2007. The power converters are connected to the current leads in the electrical distribution feed-boxes, the local current leads for orbit corrector magnets or directly to the magnet terminals of the normal-conducting magnets. Any incorrect magnet connection would seriously compromise LHC operation and is very difficult to correct, once the machine is in operation.

A rigorous Electrical Quality Assurance (ELQA) plan [16] was established for the LHC machine environment in order to ensure the safe and correct functioning of all superconducting circuits during hardware commissioning and machine operation. The steps in the electrical quality assurance are:

- Continuity, polarity, and electrical integrity verification during machine assembly.
- Measurement of electrical reference parameters at ambient temperatures for each individual electrical powering subsector.
- Online monitoring of the integrity of electrical insulation during the cool-down of the machine sector.
- Diagnostic measurements and verifications during sector commissioning and machine operation.
- Yearly verification (during shut-down periods) of cold electrical components such as the bypass diodes.
- Verification of in situ repairs of electrical circuit elements.

The photograph taken in the LHC tunnel during machine installation, Figure 1.19, shows the string of cryomagnets with an open interconnection be-

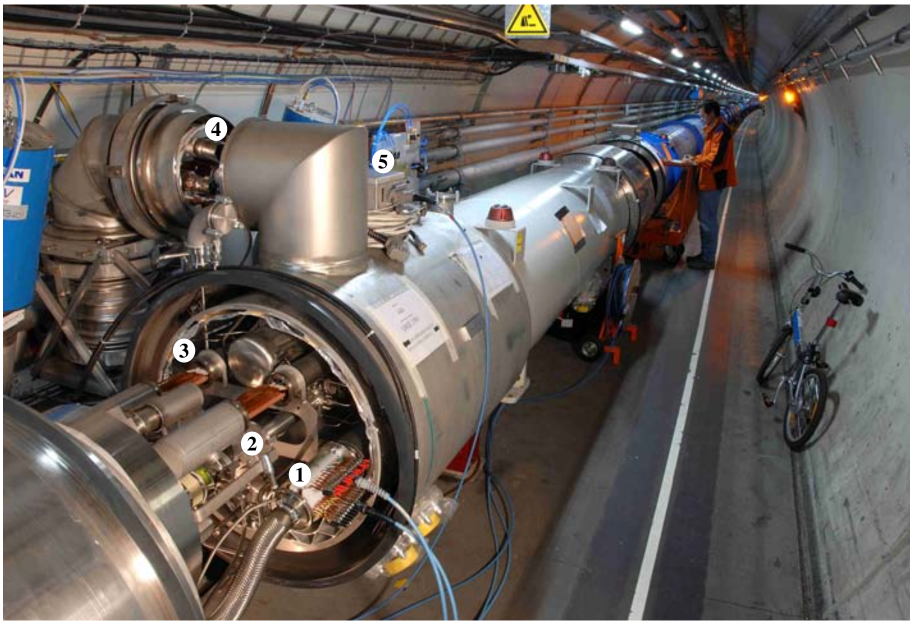

Figure 1.19 A view into the LHC tunnel during electrical tests of the interconnections between cryomagnets. (1) Interconnection board for the busbars powering the 600 A correctors in the short straight sections. (2) Beam tube. (3) Busbars for the spool piece corrector circuits. (4) Cryogenic service module. (5) Instrumentation feedthrough system.

tween them, at the time when tests were performed to verify the continuity of the electrical circuits.

Technical challenges for the power converter system result from the need to install the converters in underground areas close to the electrical feed-boxes. This is imposed by the high current rating and the inevitable ohmic heating in the water-cooled busbar systems. Only the normal-conducting magnets installed in IR 3 and 7 are powered from the surface, reusing the surface buildings and cabling from the LEP project.

Reduced-volume, high-efficiency power converters are required to fit the civil engineering infrastructure with the available radio-frequency galleries constructed for LEP. A severe design constraint was thus imposed on the Electro Magnetic Compatibility (EMC) of the equipment. The performance of the powering system is further dominated by the tolerance of 0.003 for the *Q-value*[36] of the machine. This issue arises from the segmentation of the ma-

---

[36] See Section 11.8.

chine and the nonlinear *transfer function* of the magnets.[37] A resolution and short-term stability of the power converters on the order of a few units in 10^{-6} will be needed to allow precise cycling and fine adjustment of the magnetic fields [44].

1.9
Electromagnetic Design Challenges

A full treatment of the technical challenges sketched in the previous sections could easily fill a book on its own. The challenges posed by the stringent requirements for the field quality in the accelerator magnets gave rise to R&D in the domain of analytical and numerical field computation, electromagnetic design of magnets, and mathematical optimization techniques. Documenting the experience gained, and accounting for the methodological developments undertaken, is the main objective of this book.

The ideal current distribution in a coil-dominated magnet has a $\cos n\varphi$ dependence in order to produce a pure $2n$-polar magnetic flux density in the aperture. The ideal current distribution cannot, however, be technically realized with cables and a single power supply. Therefore, the magnetic design aims at an approximation of the ideal current distribution by using cables grouped in coil blocks as shown in Figure 1.20. In order to reduce degradation of the critical current density due to the cabling process, the keystoning is usually insufficient to build up arc-segments, and therefore copper wedges are inserted between blocks of cables. The optimal size and shape of these wedges yield the degree of freedom necessary for optimizing the field quality in the magnet. Spacers of variable thickness between the collars and the coil poles, called *pole shims*, can be used to compensate for coil-size variations in the production process and thus to ensure that the dipole magnets have practically identical magnetic characteristics.

The magnetic flux density varies considerably in the coil cross section; see Figure 1.20 (left). Designing coils with two layers of cables of the same width but of different thickness allows for approximately 40% higher current density in the outer-layer cable, which is exposed to a lower magnetic field. This principle is usually referred to as *current grading*. The LHC main dipole coils are wound from cables composed of 28 Nb–Ti multifilamentary strands of 1.065 mm diameter in the inner layer and 36 strands of 0.825 mm diameter in the outer layer.

---

[37] The current to field correspondence influenced by superconductor magnetization and iron saturation.

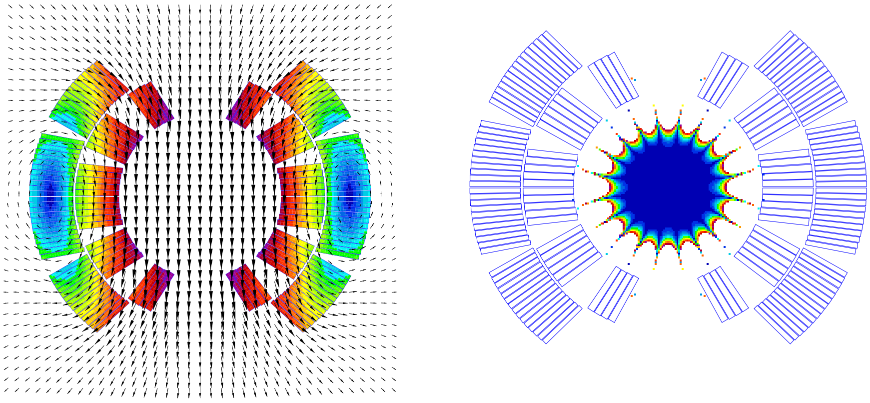

Figure 1.20 Coil cross section of an LHC model dipole [47]. Left: Field map. Right: Error on the B_y field component. $|1 - B_y/B_y^{\mathrm{nom}}| < 0.1 \times 10^{-4}$ for the dark blue areas, 2×10^{-4} maximum.

The magnetic field in the aperture of the accelerator magnets can be described either by a field map or by relative deviation from the ideal field as visualized in Figure 1.20.

Neither method illustrated in Figure 1.20 is useful for field-quality optimization. Instead, the magnetic field errors in the apertures of accelerator magnets are usually expressed by the coefficients of the Fourier[38] series expansion of the radial field component at a given reference radius: Assuming that the radial component of the magnetic flux density B_r at a given reference radius $r = r_0$ inside the aperture of a magnet is measured or calculated as a function of the angular position φ, we obtain for the Fourier series expansion of the radial field component

$$\begin{aligned} B_r(r_0, \varphi) &= \sum_{n=1}^{\infty} (B_n(r_0) \sin n\varphi + A_n(r_0) \cos n\varphi) \\ &= B_N \sum_{n=1}^{\infty} (b_n(r_0) \sin n\varphi + a_n(r_0) \cos n\varphi), \end{aligned} \tag{1.16}$$

where

$$A_n(r_0) = \frac{1}{\pi} \int_0^{2\pi} B_r(r_0, \varphi) \cos n\varphi \, \mathrm{d}\varphi, \qquad n = 1, 2, 3, \ldots, \tag{1.17}$$

$$B_n(r_0) = \frac{1}{\pi} \int_0^{2\pi} B_r(r_0, \varphi) \sin n\varphi \, \mathrm{d}\varphi, \qquad n = 1, 2, 3, \ldots. \tag{1.18}$$

---

[38] Joseph Fourier (1768–1830).

As the magnetic flux density is divergence-free, $A_0 = 0$. The B_n are called the normal and the A_n the skew field components. The physical units are $[B_n] = [A_n] = 1\,\mathrm{T}$. The b_n are the normal relative, and a_n the skew relative multipole field coefficients. The latter are dimensionless and usually given in units of 10^{-4} at a 17 mm reference radius (about 2/3 of the LHC aperture). For a good field quality these multipole components must be smaller than a few units in 10^{-4}. In the three-dimensional case, the transverse field components are integrated over the entire length of the magnet. For beam tracking it is sufficient to consider the transverse field components, since the effect of the longitudinal component of the field (present only in the magnet ends) on the particle motion can be disregarded.

Two nonlinear effects influence the multipole field components: At low field the superconducting filament magnetization results in a screening of the coil field. At high excitation the saturation of the iron yoke influences mainly the lower-order multipole coefficients.

Figure 1.21 shows the transfer function and the most sensitive quadrupole field component (intrinsic to the two-in-one design) in the main bending magnets as a function of the excitation current. Numerical methods must be used for the calculation of the saturation effects in the iron yoke.

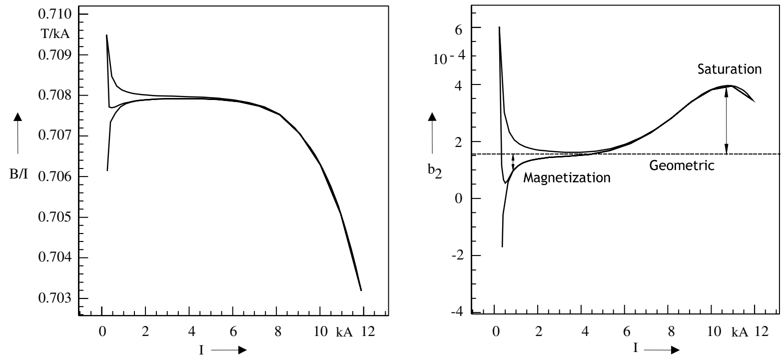

Figure 1.21 Variation in the transfer function B/I (left) and the relative quadrupole field component as a function of the excitation current (right). Notice the effect of the iron saturation at higher field levels and the superconductor magnetization at low excitation levels.

The three main sources of field errors (geometrical effects, superconductor magnetization, and time-transient effects) can be associated with three types of errors:

- Systematic errors inherent to the design geometry resulting in average errors over the whole LHC ring and in one single aperture. These errors respect the coil and magnet symmetry; no skew field components appear in the aperture field.

- Uncertainty errors arising from variations in tooling used during magnet assembly, resulting in deviations of the systematic error per magnet production line. An appropriate sorting strategy limits the impact on accelerator performance.
- Random effects due to (uncorrelated) fabrication tolerance in the different components including the superconducting strands and cables.

Systematic errors can be classified as follows:

- Errors caused by the design of the coil windings that can only approximate the ideal $\cos n\varphi$ current distribution as shown in Section 8.1.1, called geometric errors.
- Remanent fields caused by persistent currents, induced in the superconducting filaments during the ramp of the magnets to their nominal field value. Time-transient effects such as *decay* and *snap-back* [15].
- Ramp-induced eddy currents in the multistrand cables, such as interstrand coupling currents and interfilament coupling currents.
- Errors from crosstalk in the two-in-one magnet with its common iron yoke, which is asymmetric with respect to the vertical plane of the proton beam.
- Cool-down of the structure and resulting deformations of the coil geometry.
- Eddy current and magnetization effects from the beam screen.
- Stray fields in the coil-end regions, including the effect of busbars and electrical interconnections.
- Coil deformations due to electromagnetic forces.

Interstrand coupling currents are inversely proportional to the interstrand contact resistance, which is high enough for the effects to be kept under control for slow LHC ramp rates. These will however present a challenge for fast-ramping accelerators. While the geometric errors are present at each stage of the LHC excitation cycle, the persistent current effects are largest at injection energy. The saturation effects mainly affect the first higher-order multipole (b_3 in the dipole and b_6 in the quadrupole) at nominal excitation.

Uncertainty errors include:

- Systematic perturbations arising from manufacturing tooling.
- Varying properties of the superconducting cable due to different manufacturing procedures.

- Varying properties of steel in yoke and collar laminations caused by batch-to-batch variations.
- Varying assembly procedures employed by the different coldmass manufacturers.
- Torsion and sagitta of the coldmass.

The random effects mainly arise from:

- Cable placement errors due to tolerances in coil parts, for example, insulation thickness, cable keystoning, and size of copper wedges.
- Tolerances in yoke parts, for example, collar outer shape and yoke laminations.
- Manufacturing tolerances and displacements of coil blocks due to varying elastic moduli of the coils, coil winding procedure, curing, collaring, and yoking, among others.
- Tolerances in the magnet alignment.

1.9.1
The CERN Field Computation Program ROXIE

In addition to the technical challenges imposed by a large accelerator project and its magnet system, there are computational challenges for the design of magnets. As previously mentioned, the electromagnetic design and optimization of accelerator magnets is dominated by the requirement of an extremely uniform field, which is mainly defined by the layout of the superconducting coil. For the field calculation it is necessary to account for even small geometrical effects, such as those produced by the keystoning of the cable, the insulation, and coil deformations due to collaring, cool down, and electromagnetic forces. If the coils had to be modeled in the finite-element mesh, as is the case in most commercial field computation software, it would be difficult to define the current density in the keystoned cable requiring further subdivision of the coil into a number of radial layers.

For the 3D case in particular, commercial software has proven hardly appropriate for the field optimization of the superconducting LHC magnets. The ROXIE (**R**outine for the **O**ptimization of magnet **X**-sections, **I**nverse field calculation and coil **E**nd design) program package was therefore developed at CERN with the following main objectives in mind [55]:

- To write an easy-to-use program for the design of superconducting coils in two and three dimensions, taking into account field quality, quench margin, and hysteresis effects from the persistent currents.
- To provide for accurate field calculation routines that are especially suited to the investigation of superconducting magnets: accurate cal-

culation of the field harmonics, field distribution within the superconducting coil, superconductor magnetization, and dynamic effects such as interstrand and interfilament coupling currents.

- To account for the mutual interdependence of physical effects such as cable eddy currents, magnetization currents, and iron saturation.
- To integrate the program into a mathematical optimization environment for field optimization and inverse problem solving.
- To integrate the program into the engineering design procedure through interfaces to Virtual Reality, to CAD/CAM systems (for the making of drawings and manufacturing of end spacers for the coil heads), and to commercial structural analysis programs.

The modeling capabilities of the ROXIE program, together with its interfaces to CAD/CAM and its mathematical optimization routines, have inverted the classical design process wherein numerical field calculation is performed for only a limited number of numerical models that only approximate the actual engineering design. ROXIE is now used as an approach toward an integrated design of superconducting magnets. The steps of the integrated design process, including both (semi-) analytical and numerical field computation methods, are as follows:

- Feature-based geometry modeling of the coil and yoke, both in two and three dimensions, requiring only a small number of meaningful input data to be supplied by the design engineer. This is a prerequisite for addressing these data as design variables of the optimization problem.
- Conceptual coil design using a genetic algorithm, which allows the treatment of combined discrete and continuous problems (for example, the change of the number of coil windings) and solving material distribution problems. The applied niching method provides the designer with a number of local optima, which can then be studied in detail.
- Minimization of iron-induced multipoles using a finite-element method with a reduced vector-potential formulation or the coupling method between boundary and finite elements (BEM–FEM).
- Subject to a varying magnetic field, so-called *persistent currents* are generated that screen the interior of the superconducting filaments. The relative field errors caused by these currents are highest at an injection field level and must be calculated to allow a subsequent partial compensation by geometrical field errors or magnetic shims. Different iteration schemes allow the consideration of nonlinear effects due to the saturation of these shims. Deterministic search algorithms are used for the final optimization of the shims and coil cross section.
- Use of electrical network models to calculate ramp-induced losses and field errors due to so-called *interfilament* and *interstrand coupling currents*.

- Simulation of time-transient effects in quenching superconducting magnets.
- Sensitivity analysis of the optimal design by means of Lagrange-multiplier estimation and the setup of payoff tables. This provides an evaluation of the hidden resources of the design.
- Tolerance analysis by calculating Jacobi matrices and estimation of the standard deviation of the multipole field errors.
- Generation of the coil-end geometry and shape of end spacers using methods of differential geometry. Field optimization including the modeling and optimization of the asymmetric connection side, ramp and splice regions as well as external connections.
- 3D field calculation of the saturated iron yoke using the BEM–FEM coupling method.
- Production of drawings by means of a DXF interface for both the cross sections and the 3D coil-end regions.
- End-spacer manufacture by means of interfaces to CAD/CAM, supporting rapid prototyping methods (laser sinter techniques), and computer controlled five-axis milling machines.
- Tracing of manufacturing errors from measured field imperfections by the minimization of a least-squares error function using the Levenberg–Marquard optimization algorithm.

1.9.2
Analytical and Numerical Field Computation

A feasible approach to structure this book would be to group the mathematical foundations and numerical methods described in this book according to the integrated design process described above. In order not to become too application-specific, we will take the opposite approach and group the applications according to the complexity of the mathematical methods required for their solution. In this way we emphasize the universal nature of methods that can be equally well applied to other large-scale applications in electrical engineering. It also highlights the fact that a large number of subjects taught in graduate university courses on electromagnetic field theory have their role to play in real-world applications:

- Harmonic fields, Fourier series, and Legendre[39] polynomials for the postprocessing of magnetic field measurement data and the definition of the field quality.

---

[39] Adrien Marie Legendre (1752–1833).

- Green's[40] functions and the field of line-currents for the computation of coil fields in superconducting magnets.
- The image-current method for a first-order approximation of the effect of an iron yoke.
- Complex analysis methods for "back-of-the-envelope" calculations of 2D fields in the aperture of accelerator magnets.
- Numerical field computation for the calculation of iron magnetization in ferromagnetic yokes.
- Hysteresis modeling for superconducting filament magnetization.
- Coupled electromagnetic field, electric, and thermal network theory for quench simulation.
- Application of differential geometry to coil-end design.
- Mathematical optimization for shape design of coils and yokes, as well as inverse problem solving.

We will begin in the next two chapters with an introduction to linear algebra and vector analysis as foundations for the electromagnetic design of accelerator magnets.

[40] George Green (1793–1841).

References

1 Allen, J.F., Misener, A.D.: Flow of liquid helium II, Nature 141, 1938

2 Asner, A.: High Field Superconducting Magnets, Clarendon Press, Oxford, 1999

3 Asner, A., Perin, R., Wenger, W., Zerobin, F.: First NB_3Sn superconducting dipole model magnets for the LHC break the 10 Tesla field threshold, Proceedings of the Magnet Technology Conference, MT-11, 1990

4 Asner A., Petrucci, G., Resegotti, L.: Some aspects of magnet design for high-energy physics, Proceedings of the International Conference on Magnet Technology, Published by the Rutherford Laboratory, 1967

5 Andreev, N. et al.: Status of the inner triplet quadrupole program at Fermilab, IEEE-Transactions on Applied Superconductivity, 2001

6 ATLAS Technical Proposal: CERN, LHCC 94-43, 1994

7 ALICE Technical Proposal: CERN, LHCC 95-71, 1995

8 Aymar, R., Claudet, G.: Tore Supra and He II cooling of large high-field magnets, Advances in Cryogenic Engineering, 35A, 1990

9 Benvenuti, C.: A new pumping approach for the large electron positron collider (LEP), Nuclear Instruments and Methods in Physics Research, 1983

10 Ballarino, A.: Large-capacity current leads, Physica C, 2008

11 Ballarino, A., Martini, L., Mathot, S., Taylor, T., Brambilla, R.: Large scale assembly and characterization of Bi-2223 HTS conductors, Transactions on Applied Superconductivity, 2007

12 Balewski, K., Degele, D., Horlitz, G., Kaiser, H., Lierl, H., Mess, K.-H., Wolff, S., Dustmann, C.-H., Schm§ser, P., Wiik, B. H.: Cold yoke dipole magnets for HERA, IEEE Transactions on Magnetics, 1987

13 Billan, J., Henrichsen, K.N., Laeger, H., Lebrun, Ph., Perin, R., Pichler, S., Pugin, P., Resegotti, L., Rohmig, P., Tortschanoff, T., Verdier, A., Walckiers, L., Wolf, R.: The eight superconducting quadrupoles for the ISR high-luminosity insertion, Proceedings of 11th International Conference on High-Energy Accelerators, Birkhäuser, 1980

14 Bottura, L.: A practical fit for the critical surface of NbTi, 16th International Conference on Magnet Technology (MT16), Florida, USA, 1999

15 Bottura, L., Pieloni, T., Sanfilippo, S., Ambrosio, G., Bauer, P., Haverkamp, M.: A scaling law for predicting snap-back in superconducting accelerator magnets, 9th European Particle Accelerator Conference, 2004

16 Bozzini, D. et al.: Electrical quality assurance of the superconducting circuits during LHC machine assembly, 11th European Particle Accelerator Conference, 2008

17 Brechna, H.: Superconducting Magnet Systems, Springer, Berlin, 1973

18 Bryant, P.J.: Basic theory of magnetic measurements, CAS, CERN Accelerator School on Magnetic Measurement and Alignment, CERN 92-05, Geneva, 1992

19 Burla, P., King, Q., Pett, J.G.: Optimization of the current ramp for the LHC, Proceedings of the PAC Conference, New York, 1999

20 CMS Technical proposal: CERN-LHCC-94-38, 1994

21 Chorowski, M., Lebrun, Ph., Serio, L., van Weelderen, R.: Thermohydraulics of quenches and helium recovery in the LHC prototype magnet strings, Cryogenics 38, 1998

22 Dahl, P. et. al: Performance of four 4.5-m two in one superconducting R&D dipoles for the SSC, IEEE Transactions on Nuclear Science, 32, 1985

23 Devred, A.: Practical low-temperature superconductors for electromagnets, CERN Yellow Report, 2004

24 Dieterich, D.R., Godeke A.: Nb_3Sn research and development in the USA – wires and cables, Cryogenics 48, 2008

25 Edwards, H.T.: The Tevatron energy doubler: a superconducting accelerator, Annual Review of Nuclear and Particle Science 35, 1985

26 Ekin, J.W.: Superconductors, in Reed R. P., Clark, A. F. (editors): Materials at low temperatures, American Society for Metals, OH, USA, 1983

27 Evans, L.: The Large Hadron Collider: a Marvel of Technology, EPFL Press, Lausanne, Switzerland, 2009

28 Flükiger, R., Uglietti, D., Senatore, C., Buta, F.: Microstructure, composition and critical current density of superconducting Nb_3Sn wires, Cryogenics, 2008

29 Feynman, R. P.: Superfluidity and superconductivity, Review of Modern Physics, 1957

30 Gröbner, O.: Vacuum and Cryopumping, CAS School on Superconductivity and Cryogenics for Accelerators and Detectors, CERN Yellow Report 2004-008

31 Gupta, R., Ramberger, S., Russenschuck, S.: Field quality optimization in a common coil magnet design, 16th International Conference on Magnet Technology, MT16, Fl, USA, 1999

32 Gurlay, S.A. et al.: Magnet R&D for the US LHC accelerator research program (LARP), IEEE Transactions on Applied Superconductivity, 2006

33 HERA tunnel, photograph reprinted with permission from DESY.

34 Iwasa, Y.: Case Studies in Superconducting Magnets, Design and Operational Issues, Plenum, New York, 1994

35 Jain, A. K.: Harmonic coils, CERN Accelerator School on Measurement and Alignment of Accelerator and Detector Magnets, CERN Yellow Report 98-05

36 Kane, G., Pierce, A. (editors): Perspectives on LHC Physics, World Scientific, Singapore, 2008

37 Kapitza, P.: Viscosity of liquid helium below the lambda point, Nature 141, 1938

38 Kuchnir, M., Walker, R. J., Fowler, W. B., Mantsch, P. M.: Spool piece testing facility, IEEE Transactions on Nuclear Science, 1981

39 Lafferty, J.M.: Foundations of Vacuum Science and Technology, John Wiley & Sons, New York, 1998

40 Lebrun, Ph.: Cryogenics for the large hadron collider, IEEE Transactions on Applied Superconductivity, 2000

41 Lebrun, Ph., Tavian, L.: The technology of superfluid helium, in Proceedings of the CERN-CAS School on Superconductivity and Cryogenics for Accelerators and Detectors, CERN-2004-008, 2004

42 Lebrun, Ph.: Advanced technology from and for basic science: superconductivity and superfluid helium at the large hadron collider, CERN/AT 2007-30, 2007

43 LEP Design Report: CERN-LEP 84-01, 1984 and CERN-AC 96-01 (LEP2), 1996

44 LHC Design Report, Vol. 1, The LHC main ring, CERN-2004-003, 2004

45 LHCB Technical Proposal: CERN, LHCC 98-4, 1998

46 The LHC Study Group, Large Hadron Collider, The accelerator project, CERN/AC/93-03

47 The LHC study group, The Large Hadron Collider, Conceptual Design, CERN/AC/95-05

48 Lee, P. J.: http://www.asc.wisc.edu/plot/plot.htm.

49 Bon Mardion, G., Claudet, G., Vallier, J.C.: Superfluid helium bath for superconducting magnets, Proceedings of the ICEC 6, IPC Science & Technology Press, 1976

50 Meinke, R.: Superconducting magnet system for HERA, IEEE Transaction on Magnetics, 1990

51 Meß, K.H., Schmüser, P., Wolff, S.: Superconducting Accelerator Magnets, World Scientific, Singapore, 1996

52 Morgan, G.H., Green, A., Jochen, G., Morgillo, A.: Winding Mandrel design for the wide cable SSC dipole, Applied Superconductivity Conference, 1990

53 Richter, D.: Private communications, 2008

54 Royet, J.M., Scanlan, R.M.: Development of scaling rules for Rutherford type superconducting cables, IEEE Transactions on Magnetics, 1991

55 Russenschuck, S.: A computer program for the design of superconducting accelerator magnets, 11th Annual Review of Progress In Applied Computational Electromagnetics, 1995, Monterey, CA, USA. LHC-Note 354, CERN, Geneva

56 Sahner, T.: Private communications, CERN, 2009

57 Sanford, J.R., Matthews, D.M. (editors): Site-Specific Conceptual Design of the

Superconducting Super Collider, Superconducting Super Collider Laboratory, 1990

58 Sgobba, S. et al.: Cryogenic properties of special welded austenitic steels for the beam screen of the large hadron collider, Proceedings of the 4th European Conference on Advanced Materials and Processes, 1995

59 Shintomi, T. et al.: Progress of the LHC low-b quadrupole magnets for the LHC insertions, IEEE Transactions of Applied Superconductivity, 2001

60 Thompson, P.A., Gupta, R.C., Kahn, S.A., Hahn, H., Morgan, G.H., Wanderer, P.J., Willen, E.: Revised cross section for RHIC dipole magnets, Conference Record of the 1991 Particle Accelerator Conference, 1991

61 Tilley D.R., Tilley, J.: Superfluidity and Superconductivity, Adam Hilger, UK, 1990

62 Todesco, E., Völlinger, C.: Corrective Actions on the LHC main dipole coil cross-section for steering systematic b3, b5, b7, private communication, 2003

63 TOTEM: Total Cross Section, Elastic Scattering and Diffractive Dissociation at the LHC, CERN, LHC 99-7, 1999

64 Van Sciver, S.: Helium Cryogenics, Plenum, New York, 1986

65 Wiik, B.H.: Progress with HERA, IEEE Transactions on Nuclear Science, 32, 1985

66 Wille, K.: The Physics of Particle Accelerators, Oxford University Press, Oxford, 2000

67 Willen, E. et al.: Superconducting dipole magnets for the LHC insertion regions, Proceedings of the EPAC Conference, Vienna, 2000

68 Wilson, M.N.: Superconducting Magnets, Oxford Science Publications, Oxford, 1983

69 Wilson, M.N.: Private communications, 2006

70 Wilson, M.N.: NbTi superconductors with low ac losses: a review, Cryogenics 48, 2008